NASA

Technical Memorandum 84959

RADIATIVE EFFECTS OF THE EL CHICHÓN VOLCANIC ERUPTION: PRELIMINARY RESULTS CONCERNING REMOTE SENSING

El Chichón Remote Sensing Working Group (ERSWG)

Editors: W. R. Bandeen and R. S. Fraser

DECEMBER 20, 1982

National Aeronautics and Space Administration

Goddard Space Flight Center
Greenbelt, Maryland 20771

TM-84959

RADIATIVE EFFECTS OF THE EL CHICHÓN VOLCANIC ERUPTION: PRELIMINARY RESULTS CONCERNING REMOTE SENSING

El Chichón Remote Sensing Working Group (ERSWG)

December 20, 1982

National Aeronautics and
Space Administration

GODDARD SPACE FLIGHT CENTER
Greenbelt, Maryland 20771

FOREWORD

Soon after the Mexican volcano El Chichón erupted during the period March 28 to April 4, 1982—spewing large amounts of ash and gaseous products into the atmosphere—unusual effects began to appear in certain geophysical parameters determined from satellites using remote sensing techniques. For example, sea surface temperatures obtained in equatorial regions from the NOAA-7 operational satellite were observed to be too low by several degrees (°C) when compared to ship and buoy measurements, and total ozone retrievals from the Nimbus-7 satellite were observed to be unreasonably large in the vicinity of the volcanic cloud.

As a result, an ad hoc El Chichón Remote Sensing Working Group (ERSWG) was formed, consisting of scientists and engineers associated with some currently active satellite sensors, to exchange information on how the eruption was affecting the various sensors and to coordinate activities with respect to developing a more complete understanding of the event and to formulating additional plans for further research.

The purpose of this document is to combine under one cover a number of individual reports concerning the history of El Chichón eruption, a treatment of some relevant chemical and radiative processes involved, and a discussion of the expected and observed effects of the volcanic cloud on 10 currently active satellite sensors.

Coming relatively soon after the eruption, many of the discussions in this document are indeed (as the title implies) preliminary and incomplete. However, it was deemed advisable to disseminate this information as soon as possible in order to inform other workers in the field of these activities and to provide a point of departure for further research that will undoubtedly continue for a long time to come on the effects of volcanic eruptions on remote sensing.

William R. Bandeen
Chairman, ERSWG

EL CHICHÓN REMOTE SENSING WORKING GROUP (ERSWG)

NASA/GODDARD SPACE FLIGHT CENTER (GSFC)

– Laboratory for Atmospheric Sciences

1. W. R. Bandeen*
2. D. Chesters
3. M. D. Chou
4. R. S. Fraser**
5. P. Gloersen
6. M. D. King
7. J. Susskind

– Laboratory for Planetary Atmospheres

8. A. J. Krueger
9. R. W. Stewart

– Instrument Systems Division

10. J. A. Gatlin

NOAA/NATIONAL ENVIRONMENTAL SATELLITE, DATA, AND INFORMATION SERVICE (NESDIS)

– Climate and Earth Sciences Laboratory

11. A. Gruber
12. M. Matson
13. E. P. McClain
14. L. L. Stowe
15. A. F. Strong

– Satellite Experiment Laboratory

16. W. A. Hovis

SYSTEMS AND APPLIED SCIENCES CORPORATION

17. P. K. Bhartia

UNIVERSITY OF MARYLAND

18. Harshvardhan

*Chairman
**Assistant Chairman

ABSTRACT

The aerosols and gases resulting from the El Chichón volcanic eruption had, and may still have, significant effects on satellite measurements of the properties of the earth's atmosphere. The sea surface temperature measured by the AVHRR was biased up to –2.5°C for many months. The total amount of ozone derived from TOMS with a standard algorithm was greatly in excess of the possible value. This apparent excess can now be explained in terms of additional absorption by SO_2. Infrared temperature sounders have observed both positive and negative anomalies. These effects and others on many satellite measurements are addressed following a discussion of the history and composition of the ejecta remaining in the stratosphere. Finally, recommendations are made for further study to account for the effects of volcanic eruptions on satellite observations and for use of such observations to measure the characteristics of the ejecta.

CONTENTS

ILLUSTRATIONS

ILLUSTRATIONS (Cont'd)

TABLES

FIGURE CAPTIONS

Figure 3.1. Monthly mean aerosol optical depths and estimated size distributions for measurements collected at Mauna Loa Observatory during June and July 1982. The curves on the left indicate regression fit to the data using the inverted size distributions.

Figure 3.2. Aerosol optical thickness as a function of wavelength for the July 1982 stratospheric aerosol size distribution presented in Figure 3.1, where the aerosol particles are assumed to be composed of a 75% H_2SO_4 solution.

Figure 3.3. As in Figure 3.2 except for the single scattering albedo of the aerosol particles.

Figure 3.4. As in Figure 3.2 except for the asymmetry factor of the aerosol particles.

Figure 3.5. Phase function as a function of scattering angle for the July 1982 stratospheric aerosol size distribution presented in Figure 3.1, where $\lambda = 0.7\ \mu m$ and $m = 1.428 - 2.07 \times 10^{-8} i$. This phase function has an asymmetry factor $g = 0.768$ and an extinction to backscatter ratio $S = 73.3$ sr.

Figure 3.6. Degree of polarization $(I_r - I_\ell)/(I_r + I_\ell)$ as a function of scattering angle for incident unpolarized radiation and for the July 1982 stratospheric aerosol size distribution presented in Figure 3.1, where $\lambda = 0.7\ \mu m$ and $m = 1.428 - 2.07 \times 10^{-8} i$.

Figure 4.1. Difference (bias) of satellite MCSST and NOAA fixed buoy (#42003) in the Gulf of Mexico (26N, 86W) during a portion of 1982.

Figure 4.2. Negative bias distribution of monthly mean satellite MCSST from ship SST for (a) May 1982, (b) June 1982, (c) July 1982, (d) August 1982, (e) September 1982. Good correspondence has been seen between regions of negative bias and El Chichón aerosol, as observed from ground and aircraft based lidar systems.

TABLE CAPTIONS

ACRONYMS

AVHRR – Advanced Very High Resolution Radiometer

CZCS – Coastal Zone Color Scanner

ERB – Earth Radiation Budget

GLAS – Goddard Laboratory for Atmospheric Sciences

GOES – Geostationary Operational Environmental Satellite

GSFC – Goddard Space Flight Center

HIRS – High Resolution Infrared Radiation Sounder

HIRS2 – HIRS Model 2

MCSST – Multichannel Sea Surface Temperature

MCIDAS – Man Computer Interactive Data Access System

MSS – Multispectral Scanner

MSU – Microwave Sounding Unit

NASA – National Aeronautics and Space Administration

NESDIS – National Environmental Satellite, Data, and Information Service

NOAA – National Oceanic and Atmospheric Administration

QCM – Quartz Crystal Microbalance Cascade Impactor

SAMS – Stratospheric and Mesospheric Sounder

SBUV – Solar-Backscattered Ultraviolet

SME – Solar Mesospheric Explorer

SMMR – Scanning Multichannel Microwave Radiometer

SST – Sea Surface Temperature

TIROS – Television and Infra-Red Observation Satellite

TM – Thematic Mapper

TOMS – Total Ozone Mapping System

TOVS – TIROS Operational Vertical Sounder

VAS – VISSR Atmospheric Sounder

VISSR – Visible Infrared Spin-Scan Radiometer

RADIATIVE EFFECTS OF THE EL CHICHÓN VOLCANIC ERUPTION: PRELIMINARY RESULTS CONCERNING REMOTE SENSING

1. INTRODUCTION

Satellite measurements of properties of the earth and its atmosphere were seriously affected by the debris thrown into the atmosphere as a result of the massive El Chichón volcanic eruptions during the period March 28 to April 4, 1982. The volcano is located in Mexico at latitude 17.3°N and longitude 93.2°W (Fig. 1.1). Spurious estimates of total atmospheric ozone from satellite measurements were soon apparent, and difficulty in retrieving sea surface temperatures from infrared measurements has persisted. Many other satellite observations are affected, also. The purpose of this report is to make a preliminary assessment of the effects of the El Chichón atmospheric contamination on most satellite current observations of the earth and its atmosphere.

The volcanic aerosols residing in the stratosphere change the climate by modifying the radiation balance of the earth-atmosphere system. Relevant parameters resulting from the recent Mount St. Helens' eruptions have been extensively documented by Deepak (1982), in *Science*, v. 211, February, 1981, and by Newell and Deepak (1982), and for the Soufriere eruptions in *Science*, v. 216, June 4, 1982. The El Chichón aerosol is expected to cause a stronger climate effect, because more aerosols occur higher in the stratosphere where they will last longer. The current satellite observations will measure some characteristics of this stratospheric layer on a global scale.

This report is organized to follow with a discussion of the history of recent El Chichón eruptions, largely based on satellite observations. The important chemical processes in the stratospheric volcanic cloud will be reviewed. Their radiative properties and also those of the aerosols persisting in the stratosphere are discussed. Then a preliminary assessment of the effect of the El Chichón debris is made for the following satellite sensors:

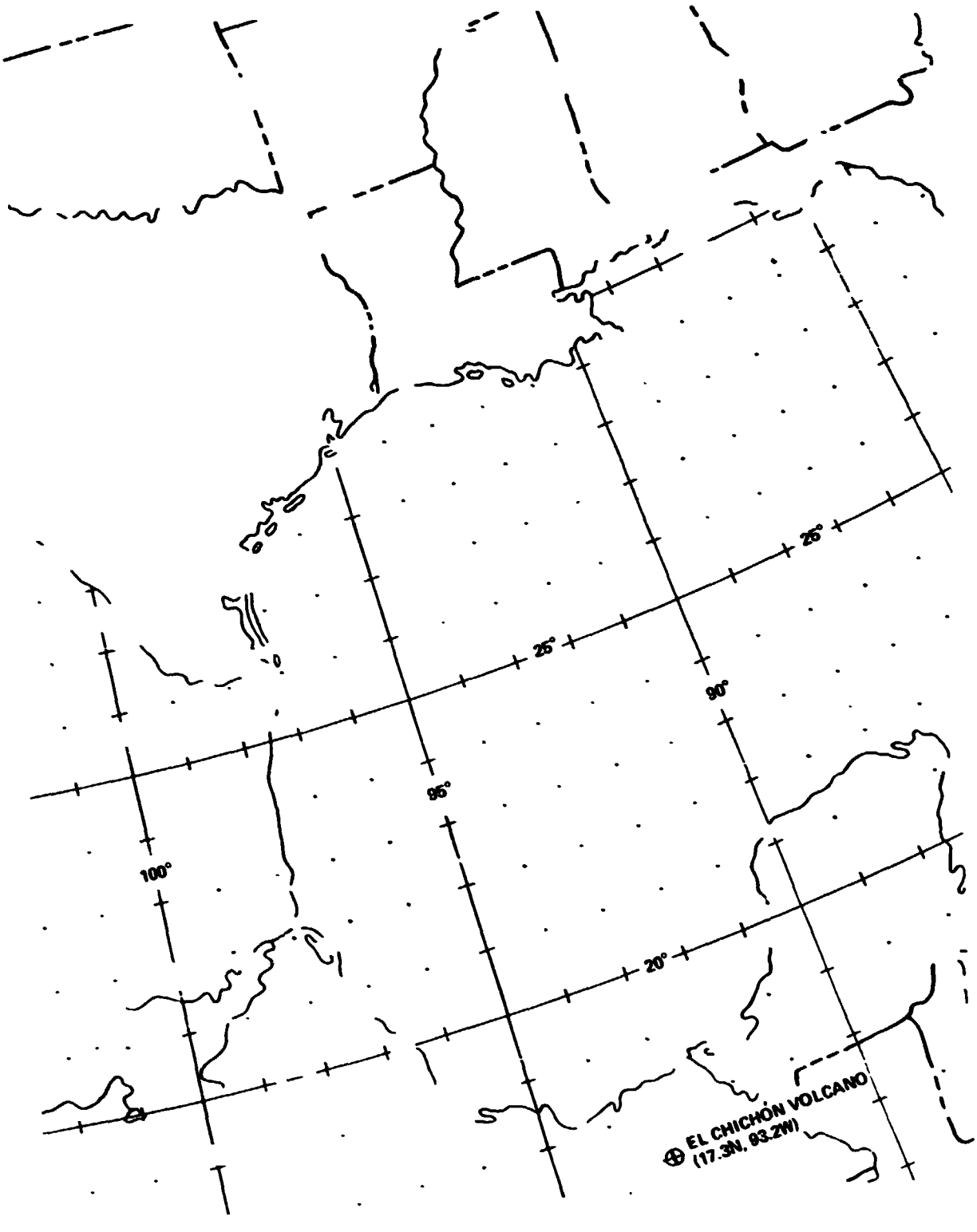

Figure 1.1. Location of El Chichón volcano.

Advanced Very High Resolution Radiometer (AVHRR) on NOAA-6 and 7, TIROS Operational Vertical Sounder (TOVS) on TIROS-N, Visible and Infrared Spin Scan Radiometer (VISSR) and the VISSR Atmospheric Sounder (VAS) on the Geostationary Operational Environmental Satellite (GOES), Solar Backscattered Ultraviolet/Total Ozone Mapping System (SBUV/TOMS) on Nimbus-7, Earth Radiation Budget (ERB) on Nimbus-7, Coastal Zone Color Scanner (CZCS) on Nimbus-7, Scanning Multichannel Microwave Radiometer (SMMR) on Nimbus-7, and the Multispectral Scanner (MSS) and Thematic Mapper (TM) on Landsat. The authors of each subsection appear at its end. Conclusions and recommendations to reduce errors in the derived parameters or for deriving new information concerning the volcanic debris are given.

References (Section 1)

Deepak, A. (Editor), 1982: Atmospheric Effects and Potential Climate Impact of the 1980 Eruptions of Mount St. Helens. NASA Conference Publication 2240, Scientific and Technical Information Branch, 303 pp.

Newell, R. E. and A. Deepak, 1982: Mount St. Helens Eruptions of 1980. NASA, Scientific and Technical Information Branch, Washington, D.C. 119 pp.

2. ERUPTIONS OF EL CHICHÓN VOLCANO

2 .. GOES AND NOAA-6 OBSERVATIONS OF EL CHICHÓN ERUPTIONS

On March 28, 1982, at 2332 local time, (add 6 hours to change to GMT) El Chichón volcano erupted violently, the first of four major eruptions. The GOES first recorded the eruption at midnight. Imagery from this satellite is acquired approximately every 30 minutes in both the visible (0.55-0.75 micrometers) and thermal infrared (10.5-12.5 micrometers) at a maximum resolution of 1 and 8 km, respectively. On March 29, at 0230, satellite digital data gave lowest eruption cloud brightness temperatures of -75.2C. Comparison with radiosonde data at Veracruz, Mexico (19.15N, 96.12W), showed that this temperature was reached at a height of 16.3 km. The Veracruz data also showed that the altitude of the tropopause was 16.5 km, thus the eruption column probably did reach the tropopause.

By 0800 the ash cloud began to dissipate, the minimum satellite-derived brightness temperatures being -63.2C at this time. The temperature corresponded to a height of 13.3 km. The ash cloud spread in a northeasterly direction, although a westerly component over the Pacific was also evident (Fig. 2.1). Upper air wind data at Veracruz showed winds from the SW between 10.4 and 15.2 km, and winds from the NE at 24 km. Thus the easterly drift was tropospheric and the Pacific component was stratospheric. By the end of the day the main ash cloud stretched from Cuba to 103W and covered an area of approximately 600,000 km^2.

At 0230 on April 3, 1982, El Chichón erupted again and the first GOES satellite recording of the event occurred at 0300. This eruption was not as large as the March 28 event. Digital data at 0400 showed minimum brightness temperatures of -71.2C, corresponding to an altitude of 15.1 km when compared to Veracruz radiosonde data. This was below the tropopause which was at 17.0 km. At 0800 -59.2C was the lowest brightness temperature recorded by the GOES data, corresponding to a height of 12.5 km. After the eruption the ash cloud spread both NE and SW (Fig. 2.2) at heights of between 13.7 to 16.3 km and 0 to 4.9 km, respectively, compared with Veracruz upper air data.

ORIGINAL PAGE
BLACK AND WHITE PHOTOGRAPH

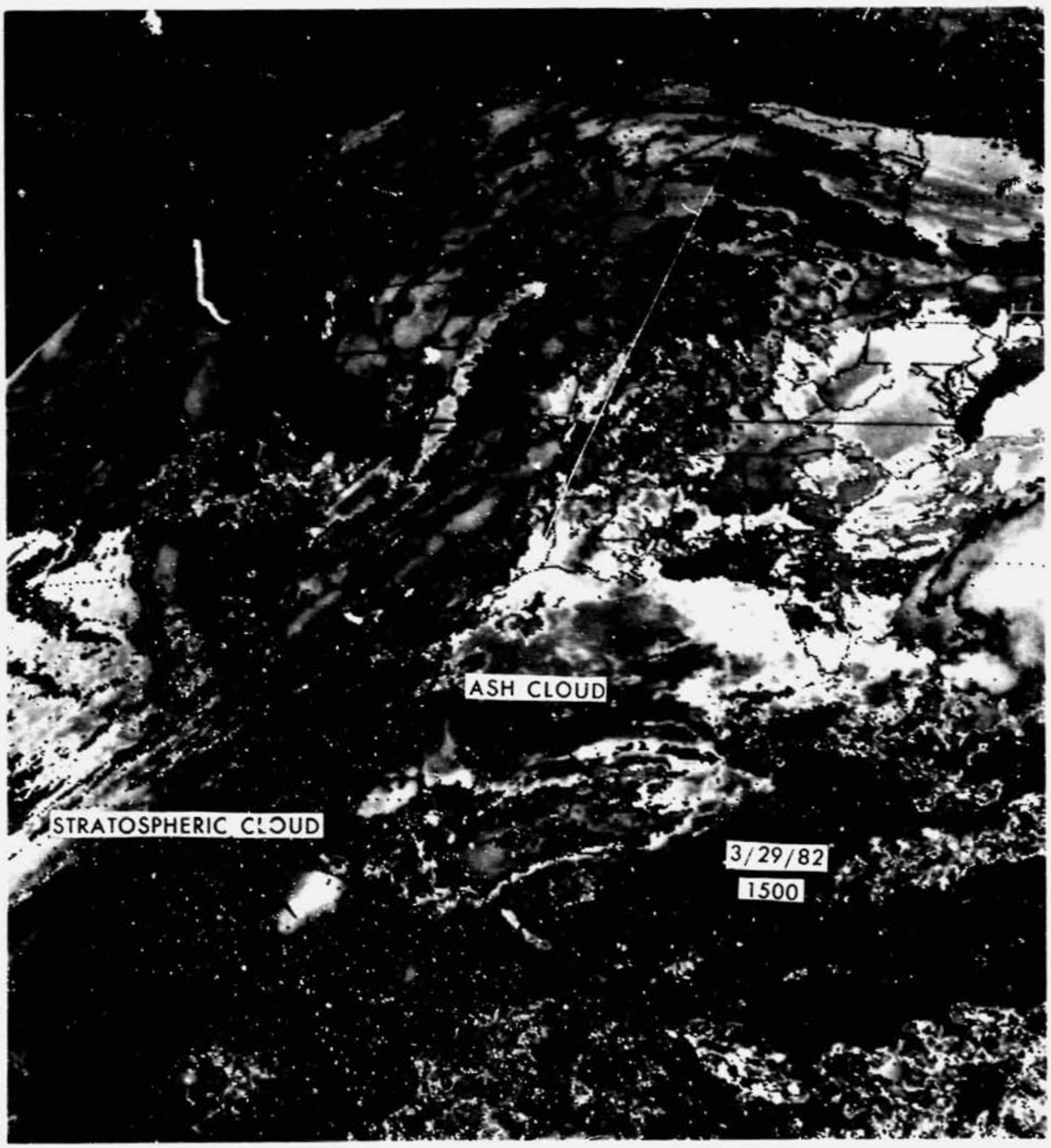

Figure 2.1. GOES enhanced thermal IR image of El Chichón ash cloud on March 29, 1982 at 1500 local time. The cloud is from the March 28 eruption at 2332 local time.

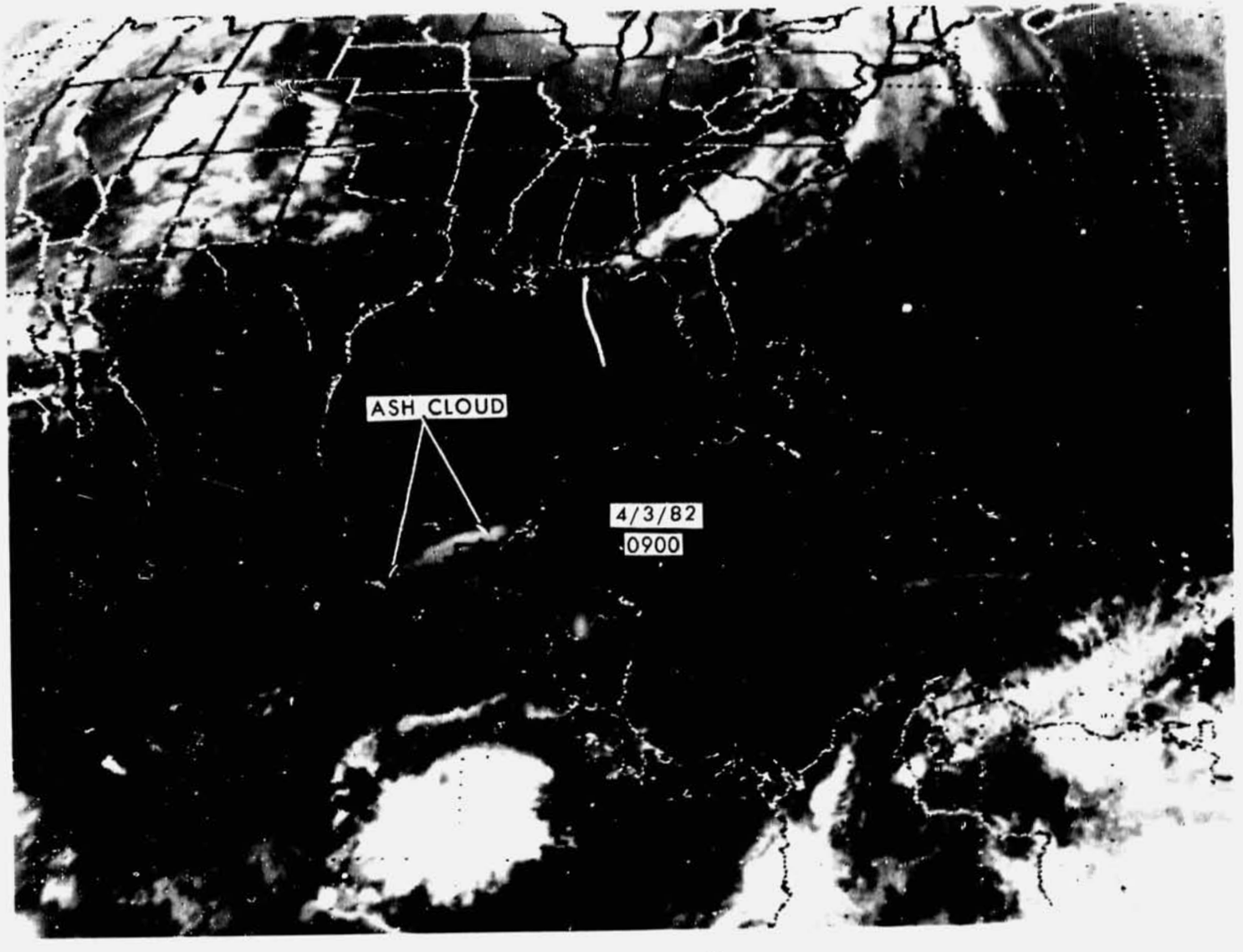

Figure 2.2 GOES unenhanced thermal IR image of El Chichón ash cloud, which was in the troposphere, on April 3, 1982 at 0900 local time. The cloud is from the second eruption at 0250 local time.

Late on April 3, 1982, and again early on April 4, 1982, there were two additional major eruptions of El Chichón, the second occurring within 10 hours of the first. The first eruption began about 2000 and the subsequent ash cloud spread over southern Mexico, Belize, and northern Guatemala (Fig. 2.3), elongated NE-SW. Upper air data at Veracruz showed stratospheric northeast winds from 20.7 to 24.0 km and tropospheric southwest winds from 13.7 to 18.5 km. At 2200 minimum satellite brightness temperatures of -78.2C were recorded, lower than the lowest radiosonde temperature of -77.5C at the tropopause (16.9 km). On April 4 at 0030 minimum satellite brightness temperatures were -71.2C, corresponding to an approximate height of 15 km.

The final and largest eruption of El Chichón began at 0522 on April 4 (Fig. 2.4). The NOAA-6 polar-orbiting satellite recorded the eruption at 0744 in both the visible band (0.58-0.68 μm) and thermal IR band (10.5-11.5 micrometers) at a resolution of 1 km. The thermal IR data showed satellite-brightness temperatures at least as low as -83.0C, a temperature below the lowest Veracruz radiosonde temperature of -75.3C at the tropopause (16.2 km). This eruption clearly penetrated the tropopause and was primarily responsible for the stratospheric cloud that subsequently circled the Earth; the beginnings of which are visible drifting westward in Fig. 2.5.

M. Matson

Figure 2.3. GOES unenhanced thermal IR image of El Chichón ash cloud between two eruptions on April 4, 1982 at 0100 local time. The cloud is from the third eruption on April 3 at 2000 local time.

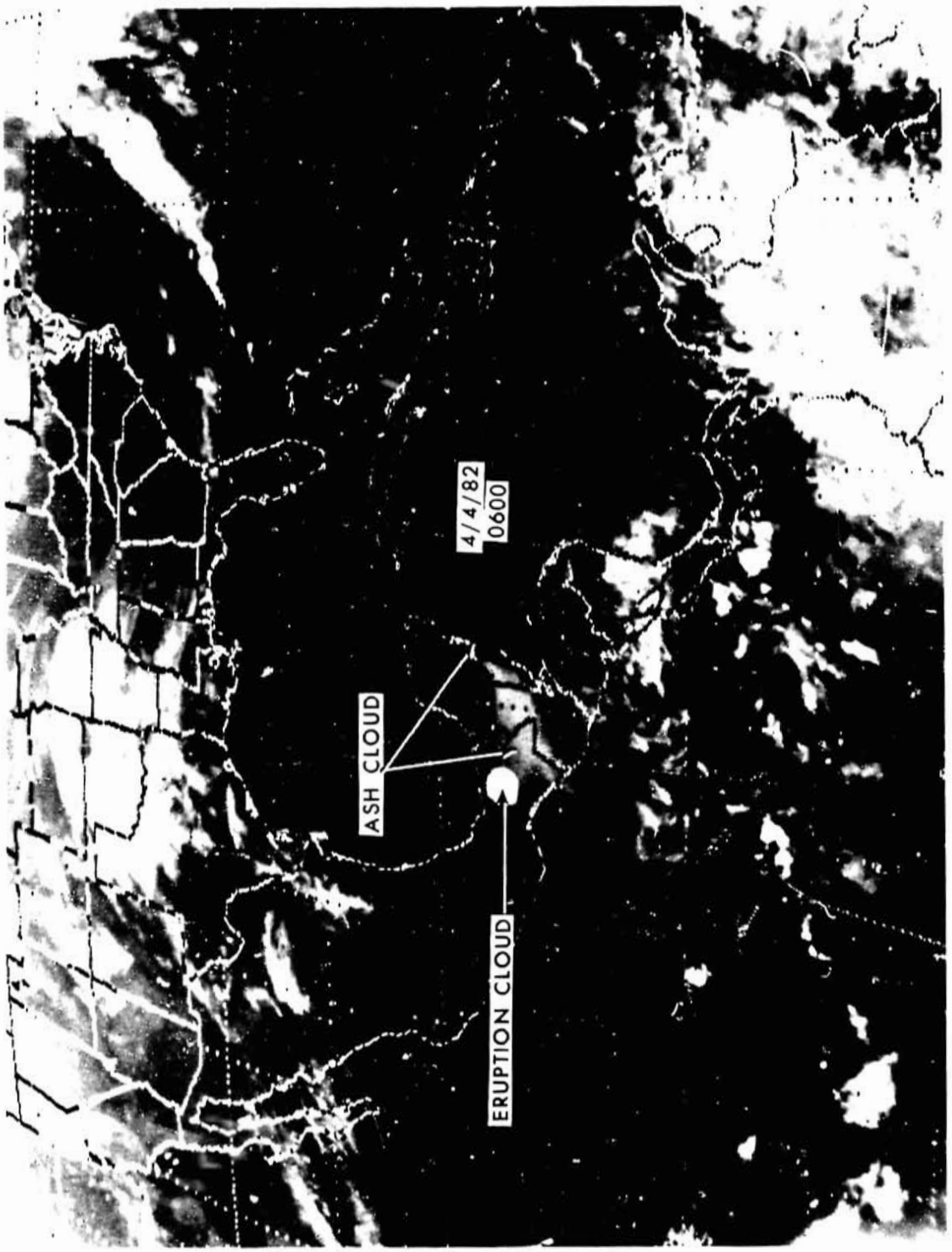

Figure 2.4. GOES unenhanced thermal IR image of the fourth El Chichón eruption on April 4, 1982 at 0600 local time. The ash cloud is from the third eruption on April 3.

ORIGINAL PAGE
BLACK AND WHITE PHOTOGRAPH

Figure 2.5. GOES unenhanced thermal IR image of El Chichón ash cloud on April 4, 1982 at 1730 local time, after the final eruption.

2.2. OBSERVATIONS OF EL CHICHÓN CLOUD CHARACTERISTICS

The eruption of El Chichón is moderately well documented compared to earlier major eruptions such as Agung and Fuego because of its relative proximity to the U.S., the availability of advanced satellite sensors, and a fortuitous passage of the early stratospheric cloud over the NOAA Mauna Loa station. In this section the various observing platforms and instruments are indicated and the initial findings are described. The SEAN Bulletins (Smithsonian Institution, 1982) contain additional information about the eruptions.

2.2.1. Observing capabilities

2.2.1.1. Operational satellites

The ash and liquid phase clouds were initially sighted from the GOES and NOAA-6 and 7 spacecraft using visible and infrared channels. The visible light observations provided information about the drift and dispersion of the clouds as described in the previous section. In addition, estimates of plume top height were derived from IR window channel temperatures as described in Section 2.1.

Effects of the cloud were found in sea surface temperatures derived from AVHRR data. Anomalously low values relative to ship observations were used to map the drift and spread of the cloud. Fig. 4.2a illustrates the affected areas during the month of May. These results are considered in more detail in section 4.1.

2.2.1.2. Research satellites

The primary research satellites in operation during El Chichón eruption were Nimbus 7 and Solar Mesospheric Explorer (SME). The sensors on Nimbus 7 of interest for eruption studies are SBUV/TOMS, Stratospheric and Mesospheric Sounder (SAMS), SMMR, ERB, and CZCS. The effects of the cloud as a contaminant to the radiances observed with the Nimbus sensors, except

for SAMS, are considered in detail in section 4. Nimbus data processing is generally delayed until definitive instrument parameters and validation studies are complete. However, in the case of TOMS the data were specially processed in near real time during the eruptions. Thus it was possible to observe the signature of the cloud immediately and to track its movement for guidance in sampling aircraft flight planning.

Strong absorption was found in the two shortest wavelength channels of 3 (Krueger, 1983). This absorption, which mimicked that of ozone in the retrievals, was to be due to sulfur dioxide. Figure 2.6 illustrates the SO_2 cloud on April 6, approximately two days after the major eruption. This false color map of total ozone shows a region of brown colors surrounding a black area extending east and west from the volcano located in southern Mexico. The black color indicates invalid ozone retrievals due to the SO_2 in the cloud. On this day the cloud was almost completely sheared into an eastward-drifting tropospheric component and a westward-drifting stratospheric component. The tropospheric cloud was found to disappear within six days while the stratospheric cloud persisted and evolved slowly in shape due to wind shear.

The El Chichón cloud was observed by three sensors on the SME spacecraft. The visible light spectrometer which observed the atmospheric limb radiance in the 400 nm region found enhanced scattering at latitudes near that of the volcano. Radiance perturbations were also found with the Near Infrared Airglow Spectrometer at 1.27 and 1.87 μm and the Infrared Radiometer at 6.3 and 9.6 μm. These sightings show the cloud to expand to cover the zone from the equator to about 30°N and to spread in altitude in the first three months after the eruption.

2.2.1.3 Airborne sampling surveys

Research aircraft from the Aerosol Climatic Effects (ACE) and Airstream Programs were deployed soon after the El Chichón eruption. While the less energetic Mount St. Helens plume

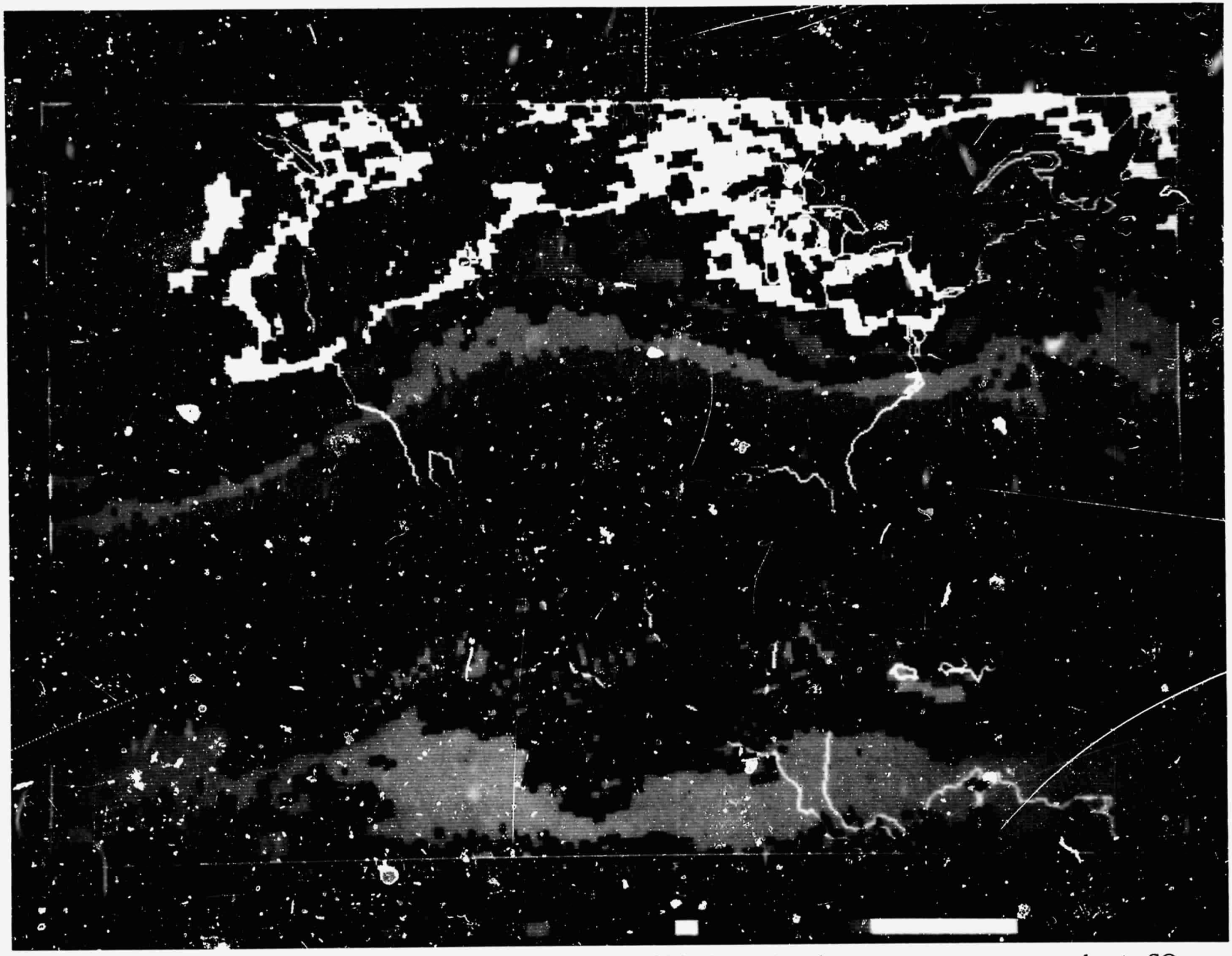

Figure 2.6. TOMS total ozone map for 1230 LT, April 6, 1982 illustrating the apparent ozone excess due to SO_2 absorption in the El Chichón cloud. The color scale for total amount of ozone is given along the bottom.

was very successfully sampled with aircraft, the primary cloud from El Chichón was about six kilometers above the peak aircraft flight altitude. Nevertheless, valuable data were collected in secondary cloud layers and in the fallout from the primary cloud. Seven ACE sampling flights were conducted in April, May, and July 1982, and pre-eruption data were obtained in March. The ACE aircraft generally were equipped with the following instrumentation:

1. Aerosol samples
   - Knollenger Particle Size Spectrometer
   - Ames Wire Impactor
   - Quartz Crystal Microbalance Cascade Impactor (QCM)
   - Condensation Nuclei Counter (University of Minnesota)
   - Filter Collector
2. Gaseous composition
   - Cryogenic cell
   - Lyman-α water vapor absorption cell

The Airstream aircraft are equipped to obtain ambient air samples for laboratory analysis of trace gases and to collect aerosols with an impactor.

2.2.1.4 Airborne lidar

Information about the height and latitudinal extent of El Chichón cloud was obtained during flights of the Langley Research Center (LaRC) airborne lidar in July and October 1982.

The July data, illustrated in Fig. 2.7, show that the primary cloud at 26 km had not spread beyond 30°N. In the second mission the cloud boundaries were at 35°N and 10°S.

2.2.1.5. Surface observations

The El Chichón cloud fortuitously passed over the NOAA station at Mauna Loa about five days after the eruptions. This station is equipped to measure atmospheric spectral transmission, diffuse skylight, total ozone, and aerosol vertical distribution. The sensors used for these observations are:

- NOAA Environmental Research Laboratory (ERL) Sun Photometer
- Eppley Normal Incidence Photometer
- Eppley Pyrheliometer
- Dobson Spectrophotometer
- Ruby lidar

In addition to these a Canadian Atmospheric Environment Service – Brewer instrument was brought in after the eruption to measure column SO_2.

Additional lidar observations are available from Fukuoka, Japan (33.65°N, 130.35°E), Langley, VA (37.1°N, 76.3°W), L'Aguila, Italy (42.37°N, 13.4°E), and Garmisch-Partenkirchen, West Germany (47.5°N, 11.0°E).

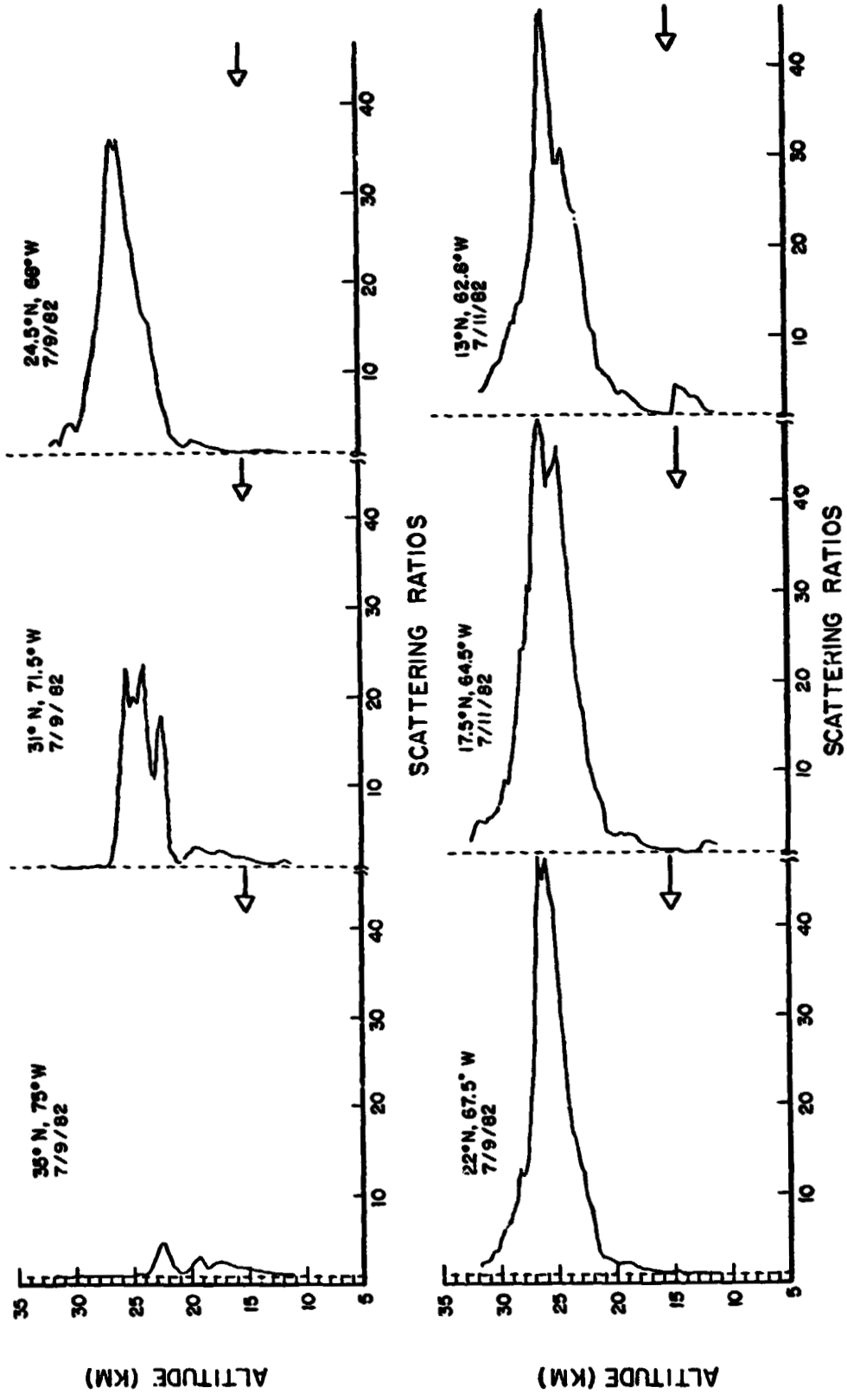

Figure 2.7. Langley Research Center lidar measurements of the ratio of the lidar to molecular back-scatter intensity of El Chichón aerosol profile from 35°N to 13°N in July 1982. The arrows indicate the height of the tropopause.

2.2.2. Cloud altitudes

Some information about cloud altitude is available from wind data. Stratospheric winds were approaching the peak of the easterly phase of the quasi-biennial oscillation (QBO). while mid-tropospheric winds were westerly. The null point between these wind regimes from Hilo radiosondes was near 21 km. Thus a crude altitude discrimination is obtained from the drift directions of the cloud volumes.

The northern part of the stratospheric cloud, according to TOMS and AVHRR analyses, drifted over Hawaii where detailed height data on the aerosol component was obtained with lidar soundings beginning at 0600 GMT, April 10. The primary layer was found at 25-26 km with secondary layers at 22 and 23.7 km. A persistent cloud top at 26 km was found during succeeding observations on April 11 and 14. The lidar returns decreased to pre-eruption levels on April 23 and strengthened again after May 5 as the cloud presumably completed its drift around the world. These and succeeding soundings exhibited a peak near 27 km and a broader height distribution than on the initial transit. Lidar data from Fukuoka, Japan (33.65°N) beginning in May and the Langley lidar survey flight in July confirm that the layer with the greatest backscatter ratio is near 26 km.

2.2.3. Cloud composition

The primary cloud layer at 26 km could not be directly sampled from aircraft due to its height. However, lower altitude layers and fallout from the upper layer were sampled during Ames ACE and DOE Airstream flights. Particles collected with the Particle Size Spectrometer and QCM cascade impactor over Baja California on April 19 consisted primarily of acid-coated silicates peaking in number at 2 μm diameter with a total mass loading of 1-4 $\mu g/m^3$. Ash particles collected on slides were found in large clusters. Sulfate particles collected by the Ames Wire Impactor were about 0.8 μm in diameter with a density of 0.6 $\mu g/m^3$. The highest sulfate concentrations (~ 160 parts per billion by mass (ppbm) as compared with a normal value of 1-2 ppbm) ever collected in 10 years of data

were found during an Airstream flight on April 15. The concentrations of condensation nuclei was found to be larger than background levels at the edges of the cloud.

Gaseous components, obtained on several Ames flights by a cryogenic collector, were analysed for SO_2, COS, and CO_2. All SO_2 mixing ratios were low (50×10^{-12}) in April, although values greater than 100×10^{-12} were found above 21.8 km in a later flight in July. The COS distribution was unusually high with 350×10^{-12} found at 19 km on May 5. Airstream gas samples, however, showed no increase in COS up to 20 km.

Water vapor was measured by Ly α absorption and showed an increase to 5 ppm compared with the long-term tropical average of 4.4 ± 0.4 ppm at 19-20 km.

Column SO_2 was measured using Brewer spectrophotometers (Evans, 1982) at Mauna Loa beginning a few weeks after the eruption and on Ames CV-990 flights in May. These measurements generally indicate elevated SO_2 amounts of 10-16 m atm cm at Mauna Loa and 5-8 m atm cm at latitudes from 20-33°N during the Ames flight. However, pre-eruption measurements from Jamaica also indicated 8 m atm cm SO_2. Thus, the SO_2 contribution by El Chichón is questionable in this data set. Later flights of this instrument on Airstream flights in July also found SO_2 column amounts of 10 m atm cm at Houston and 20 m atm cm near the Equator.

The sulfur dioxide content of the initial cloud was measured with the Nimbus-7 TOMS, since SO_2 constitutes an interfering gas, which can be discriminated from ozone by the spatial signature of the cloud. Peak column SO_2 amounts during the first days after each major eruption were about 60 m atm cm. The total SO_2 content, obtained by integrating across the cloud, was $3\text{-}4 \times 10^6$ tons for the April 4 eruption. This SO_2 amount is considerably smaller than estimates derived from the Evans' data.

2.2.4. Cloud optical properties

The optical thickness of the El Chichón cloud over Mauna Loa was measured using sun photometers (DeLuisi et al., 1982) as shown in Fig. 2.8. In the initial passage of the cloud between April 9 and 20, dust optical depths from 0.6 to 0.75 were found at 425 nm. The optical depth briefly dipped to near background levels (<0.1) on April 22-23, then returned to levels near 0.3 after April 27. The dust then slowly diminished to optical depths near 0.25 by July. The optical depths vary with wavelength, depending upon the chemical composition and size distribution, which change with time. King used this characteristic to deduce particle size distributions as discussed in section 3.2

A. J. Krueger

References (Section 2.2)

DeLuisi, J., E. Dutton, B. Merdonca and M. King, 1982: Some radiative characteristics of the El Chichón dust cloud deduced from solar radiation measurements at Mauna Loa, Hawaii. Proc. AGU Fall Meeting, San Francisco, CA.

Evans, W. F. J., 1982: Unpublished report.

Krueger, A. J., 1983: Sighting of El Chichón sulfur dioxide clouds with the Nimbus-7 total ozone mapping spectrometer, Science (in press).

Smithsonian Institution, Scientific Event Alert Network (SEAN) Bulletin, 9, No. 3-9, March-September, 1982.

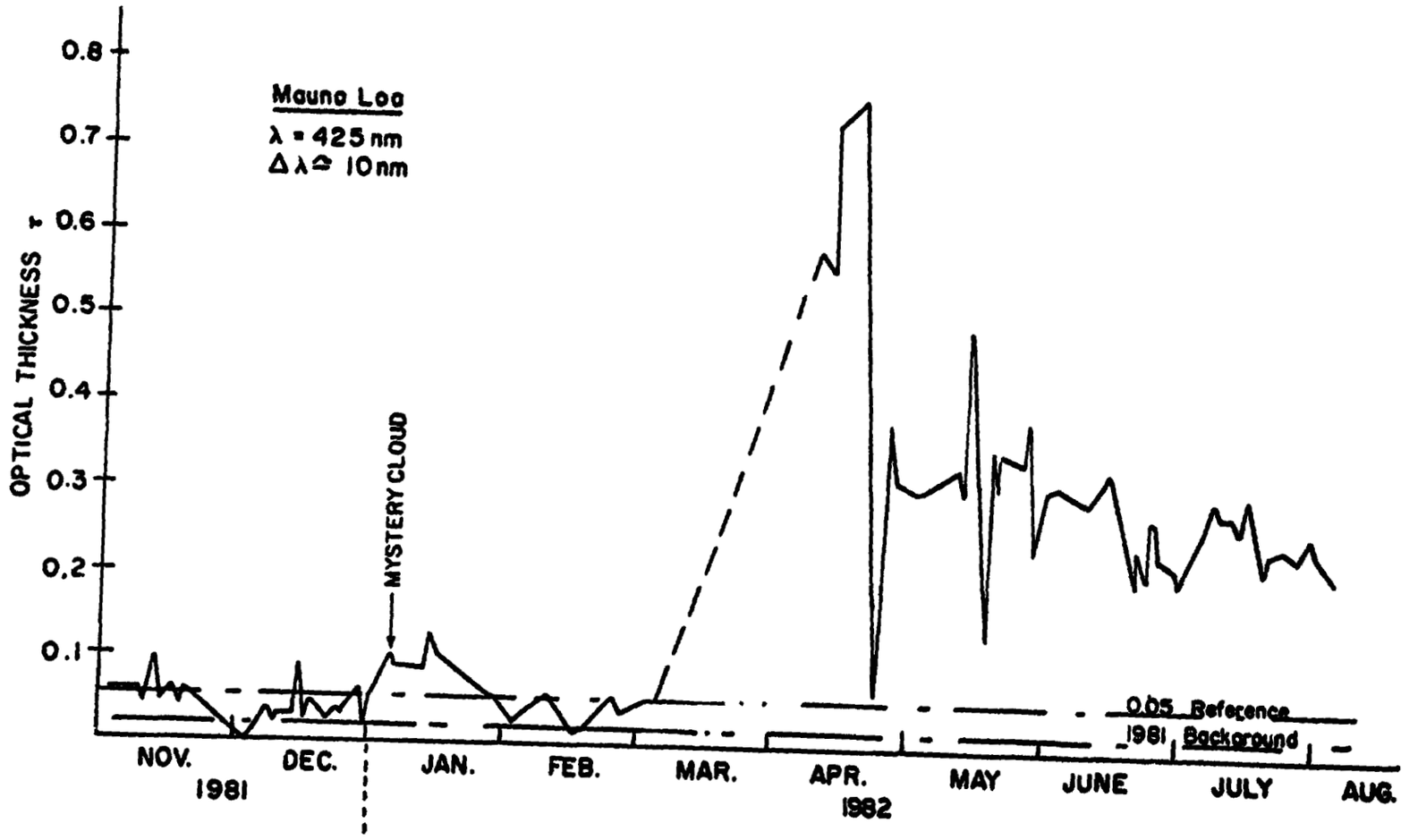

Figure 2.8. Optical thickness of stratospheric aerosols measured with a sun photometer at Mauna Loa, Hawaii, by J. DeLuisi. The wavelength is 425 nm, and the bandwidth is 10 nm.

2.3. SUMMARY OF SULFUR OXIDATION PROCESSES

2.3.1. Introduction

Sulfur compounds enter the atmosphere from anthropogenic and biological activities, sea salts, and volcanic emissions. On average, volcanoes may contribute about one third of the total sulfur emitted to the atmosphere, principally in the form of sulfur dioxide (Cadle, 1980). Local and regional concentrations of sulfur may greatly exceed those normally found in the atmosphere during and following volcanic eruptions. The constituents emitted by volcanoes are sulfur dioxide (SO_2), hydrogen sulfide (H_2S), carbonyl sulfide (COS), and carbon disulfide (CS_2). Of these, SO_2 is normally the most abundant and is found in the emissions of all volcanoes. Table 2.1 from Turco et al. (1982) gives the concentrations of sulfur compounds measured in the Mount St. Helens' plume and there is no reason to suspect that these relative amounts are other than typical. Once emitted into the atmosphere, all further chemical processes affecting sulfur are such as to produce higher oxidation states ending finally in the production of sulfate. The general nature of these processes may be classified as homogeneous gas-phase chemistry or as heterogeneous processes involving liquid phase or surface reactions. In no case is the complete oxidation sequence well understood, but several steps are either known or believed to be important. These will be summarized below.

2.3.2. Gas phase oxidation of sulfur

Gas phase chemistry provides the principal mechanisms for the oxidation of reduced sulfur to SO_2 and may contribute to the further oxidation of SO_2 to sulfate. Table 2.2 lists reactions of known or potential importance to these processes. The reactions R7 and R8 are functions of temperature, which is expressed in degrees Kelvin. Graedel in the reference column refers to Graedel's (1977) review paper that cites the original references for the various reaction rates.

The most highly reduced sulfur compound emitted from volcanoes is hydrogen sulfide. It is usually emitted in much smaller quantities than is SO_2 and is relatively rapidly oxidized in the

Table 2.1
Composition of the Emissions of Mt. St. Helens.
The Abundance Concentrations Are Expressed in Fractional Volumes

Emitted Species	Principal Roles	Relative Abundances		
		Ambient Air[1]	Fumarolic[2]	Stratospheric Plume[3]
H_2O	Cloud formation, initiate HO_x chemistry, washout of $SO_4^=$, Cl^- and NO_3	$3\text{-}5 \times 10^{-6}$	$\sim 10^{-2}$	$\sim 10^{-4}$
SO_2	Precursors of sulfate aerosols	$\sim 5 \times 10^{-11}$	$\sim 10^{-5}$	$\sim 10^{-7}$
H_2S	Consume OH radicals	$< 10^{-9}$		$< 10^{-9}$
COS		$1\text{-}5 \times 10^{-10}$		$\sim 10^{-9}$
CS_2		$\lesssim 10^{-12}$		$\lesssim 10^{-10}$
HCl	Ozone catalysis	$\sim 10^{-10}$	$\sim 10^{-5}$	$\lesssim 10^{-9}$
CH_3Cl		$\sim 10^{-10}$		$\sim 10^{-9}$
CH_3Br		$\sim 10^{-11}$		—
S/Cl[4]		$\sim 0.1 - 1.0$	~ 1.0	1.0 - 100.0
CO_2	Infrared transmission	3.6×10^{-4}	$\sim 3.6 \times 10^{-4}$	3.6×10^{-4}
CO	Tracer of OH	$\sim 10^{-8}$	?	$\sim 10^{-7}$
NH_3	Aerosol reactions	$\lesssim 10^{-10}$	?	—
N_2O	Precursor of NO_x	$\sim 10^{-7}$		$\sim 10^{-7}$
NO_x	Active in ozone cycles	$\lesssim 10^{-8}$		$\sim 10^{-8}$

1. Air in the lower stratosphere. The source of information is Hudson and Reed (1979).
2. Clouds near the volcano. Data sources are given in the text.
3. See the text for a discussion of the stratospheric data.
4. Molar ratio, for gases plus particles.

Table 2.2
Gas Phase Oxidation of Sulfur Compounds
(The numbers in parentheses are exponents to the base 10)

	Reaction	Rate ($cm^3\ sec^{-1}$)	Reference
R1)	$H_2S + OH \rightarrow HS + H_2O$	4.2 (–12)	WMO
R2)	$HS + O_2 \rightarrow SO + OH$	<1 (–13)	Graedel
R3)	$HS + O \rightarrow SO + H$	1.6 (–10)	Graedel
R4)	$SO + O_2 \rightarrow SO_2 + O$	2.7 (–17)	Graedel
R5)	$SO + NO_2 \rightarrow SO_2 + NO$	8.3 (–12)	Graedel
R6)	$CS_2 + OH \rightarrow$ Products	<1.5 (–15)	WMO
R7)	$CS_2 + O \rightarrow CS + SO$	$2.4 (-11) \times e^{-530/T}$	WMO
R8)	$COS + O \rightarrow CO + SO$	$2.1 (-11) \times e^{-2200/T}$	WMO
R9)	$SO_2 + OH \rightarrow HSO_3$	6.7 (–13)	Graedel
R10)	$SO_2 + HO_2 \rightarrow SO_3 + OH$	9.0 (–16)	Graedel
R11)	$SO_2 + CH_3O_2 \rightarrow SO_3 + CH_3O$	<3.3 (–15)	Graedel
R12)	$SO_3 + H_2O \rightarrow H_2SO_4$	1.0 (–12)	Graedel

atmosphere. The lifetime against oxidation by OH is about a day. Once the thyil radical (HS) is formed it is in turn rapidly oxidized to sulfur monoxide (SO), reactions R2 and R3 of Table 2.2. The final step in the oxidation of H_2S to SO_2 is oxidation of SO by O_2 or NO_2 and this is essentially instantaneous.

Carbonyl sulfide and carbon disulfide are much longer lived species than is hydrogen sulfide, though the oxidation rates are not yet well known. Both of these species may persist for times in excess of a month. It is unlikely that any of these reduced sulfur compounds are emitted in sufficient quantities to contribute significantly to the production of SO_2 and sulfate in a volcanic plume.

Sulfur dioxide is the predominant sulfur species emitted by volcanoes. Production of sulfuric acid and sulfates may occur to some extent through gas phase chemistry. The initial steps are oxidation of SO_2 by the odd-hydrogen radicals OH and HO_2, reactions R9 and R10 of Table 2.2. There are additional possible gas phase reactions involving production and reaction of HSOx radicals, with x equal to 3-6 (Davis, 1979), but these are speculative and are not listed in Table 2.2. It is likely that heterogeneous processes play the major role in oxidation of SO_2.

2.3.3. Heterogeneous oxidation of SO_2

Table 2.3 shows some of the liquid phase reactions involved in conversion of SO_2 to sulfate in droplets. The equilibrium constants for the reversible reactions shown in the table are the ratios of reactants to products, all expressed in units of moles/liter. The Adamowicz (1979) reference lists various aspects of the liquid phase oxidation of SO_2.

Table 2.3
Liquid Phase Oxidation of Sulfur
(The numbers in parentheses are exponents to the base 10)

	Reaction	Equilibrium Constant	Reference
R1)	$(SO_2)_g \leftrightarrow (SO_2)_\ell$	3.3 (–2)	Adamowicz
R2)	$(SO_2)_\ell \leftrightarrow H^+ + HSO_3^-$	1.7 (–2) moles ℓ^{-1}	Adamowicz
R3)	$HSO_3^- \leftrightarrow H^+ + SO_3^=$	6 2 (–8) moles ℓ^{-1}	Adamowicz
R4)	HSO_3^- (tm) $\rightarrow SO_4^=$		
R5)	$SO_3^=$ (tm) $\rightarrow SO_4^=$		
R6)	$H_2SO_4 \leftrightarrow H^+ + HSO_4^-$	0.4 moles ℓ^{-1}	Adamowicz
R7)	$HSO_4^- \leftrightarrow H^+ + SO_4^=$	1.2 (–2) moles ℓ^{-1}	Adamowicz
R8)	$HSO_3^- + O_3 \rightarrow HSO_4^- + O_2$		Turco et al.
R9)	$HSO_3^- + H_2O_2 \rightarrow HSO_3^-O + H_2O$		Turco et al.

(tm) above refers to trace metal catalysis.
The subscripts g and ℓ on (SO_2) refer to gas and liquid phase concentrations.

An outstanding problem in this area is the mechanism by which trace metals catalyze the oxidation of bisulfite (HSO_3^-) and sulfite ($SO_3^=$). These processes are indicated schematically by R4) and R5) in Table 2.3. Another difficulty in describing the liquid phase oxidation of SO_2 is the fact that strong oxidants such as H_2O_2 and, to a lesser extent, O_3 are observed to significantly enhance the rate of production of sulfate (reactions R8 to R10). SO_2 absorption, and the subsequent equilibria of sulfur species in liquid drops are pH dependent. The presence of ammonia or other bases in the atmosphere may thus increase the capacity of liquid droplets for sulfur uptake.

Reaction of SO_2 on the surfaces of suspended particles is another heterogeneous process influencing the rate of sulfur oxidation. The process is usually described in terms of a measured reaction efficiency for various solid materials. The details of the oxidation mechanism are not known and the terms representing this process in model calculations are empirical.

Because of the dependence of heterogeneous oxidation of sulfur on factors such as the presence of trace metal catalysts, strong oxidants, base constituents, and the variety of solid surfaces present, a detailed theoretical description of particular episodes of SO_2 oxidation in the eruption plumes of volcanoes is difficult. A study of SO_2 oxidation in the Mt. St. Helens' plume has recently been carried out by Turco et al. (1982), however.

P. W. Stewart

References (Section 2.3)

Adamowicz, R. F., 1979: A model for the reversible washout of sulfur dioxide, ammonia, and carbon dioxide from a polluted atmosphere and the production of sulfates in raindrops. Atmos. Environ., 13, 105-121.

Cadle, R. D., 1980: A comparison of volcanic with other fluxes of atmospheric trace gases. Rev. Geophys. and Space Phys., 18, 746-752.

Davis, D. D., A. R. Ravishankara, and S. Fischer, 1979: SO_2 oxidation via the hydroxyl radical: Atmospheric fate of HSOx radicals. Geophys. Res. Lett., 6, 113-116.

Graedel, T. E., 1977: The homogeneous chemistry of atmospheric sulfur. Rev. Geophys. and Space Phys., 15, 421-428.

Turco, R. P., O. B. Toon, R. C. Whi.ten, R. G. Keesee, and P. Hamill, 1982: The Mt. St. Helens eruptions of May and June 1980: Simulation studies of the physical and chemical processes occuring in the stratospheric clouds. Preprint, 1982.

World Meteorological Organization (WMO), 1981: The stratosphere 1981 theory and measurements, WMO rept. no. 11. Appendix A.

3. RADIATIVE CHARACTERISTICS

3.1. THEORY OF RADIATION

The qualitative effects of the El Chichón stratospheric cloud of aerosols and gases on radiances measured at a satellite can be deduced from a solution to the equation of radiative transfer:

$$I(O, \lambda, \theta, \phi) = I(t_b, \lambda, \phi)\, e^{-t_b \sec\theta} + \int_0^{t_b} J(t, \lambda, \theta, \phi) \exp(-t \sec\theta) \sec\theta \, dt, \quad (1)$$

where $I(0, \lambda, \theta, \phi)$ is the specific intensity, or spectral radiance, of the radiant energy at the aperture of a satellite radiometer; the first independent variable within parenthesis represents distance above the surface of the earth. It is expressed in terms of optical thickness (t), which increases from 0 at the top of the atmosphere to t_b at the base of the atmosphere. The other independent variables are λ for wavelength, and θ and ϕ give the zenith and azimuthal angles, respectively, of the direction that the radiation is propagating.

The first term on the right-hand side of Eq. (1) represents the intensity at the surface, but attenuated along the slant path to a satellite. The atmospheric residue from the volcano increases this attenuation, as well as altering the intensity of the sunlight transmitted to the surface to be subsequently reflected. The second term on the right-hand-side of Eq. (1) contains the source function (J), which accounts for radiant energy added along the line-of-sight. The volcanic residue in the atmosphere can contribute to J by both scattering and thermal emission processes

Further insight in the nature of the radiation sources is gained by giving the complete equation for the source function:

$$J(t, \lambda, \theta, \psi) = \omega_0(t, \lambda) \left[\frac{p}{4\pi}(t, \lambda, \theta, \phi, \theta_0, \phi_0) \times \right.$$

$$S_0(\lambda)\, e^{-t \sec \theta_0} + \int_0^{2\pi} \int_0^{\pi} \frac{p}{4\pi}(t, \lambda, \theta, \phi\ \hat{v}', \phi') \times$$

$$\left. I(\tau, \lambda, \theta', \phi') \sin\theta'\, d\theta'\, d\phi' \right] + (1 - \omega_0)\, B(T(t), \lambda), \qquad (2,$$

where ω_0 is the albedo of single scattering, or the ratio of the scattering and extinction coefficients; $(1 - \omega_0)$ gives the probability of absorption, and also for emission when the atmosphere is in local thermodynamic equilibrium. The dependent variables for the scattering phase function $(p/4\pi)$ are arranged such that the first pair of polar angles give the direction in which the energy is scattered and the last pair of angles give the direction of the incident pencil of energy. B is the Planck function at level t where the air temperature is T.

The terms within the square brackets (times ω_0) of Eq. (2) account for the scattered energy. The first of these terms gives the contribution of the direct sunlight, and the other term gives the contribution of the diffuse radiant energy arriving from all directions (θ', ϕ') and scattered in the direction (θ, ϕ). The last term (outside of the brackets) accounts for the thermal emission.

A month or so after the last El Chichón eruption, lidar scattering from the aerosols indicated that the El Chichón cloud was confined to the layer between 18 and 35 km, with peak concentration near 26 km. The trace gases from the volcano are of such low concentration that their scattering effects can be neglected. The gases absorb and emit energy, however. As will be shown in section 3.2, the aerosol particles are of submicron size. They strongly scatter light in the visible and ultraviolet spectrum; but his effect decreases in the infrared, while their absorption increases.

The vertical profile of the source function depends on the profiles of the absorbing and scattering constituents. If under normal conditions the source function peaks high in the stratosphere

and is zero below 35 km, then the volcanic cloud does not affect the radiant energy reaching a satellite. Such is the case for $\lambda < 290$ nm in the SBUV experiment. Generally, however, the source functions indicate a stratospheric response at or well below 26 km under normal conditions (see Figs. 4.4 to 4.6). Then the volcanic layer will modify the source function and affect the radiant energy coming from the earth and atmosphere. The magnitude of the effect depends on wavelength and will be discussed in the following sections.

R. S. Fraser

3.2. RADIATIVE CHARACTERISTICS OF THE AEROSOLS

The effect of aerosols from the El Chichón eruptions on satellite remote sensing depends primarily on their optical thickness, phase function, and refractive index. After a few weeks these aerosols are restricted to the stratosphere. For some remote sensing experiments, such as limb scanners or solar occultation observations the vertical distribution of the aerosol layer will also play a key role in modifying the radiation field at satellite altitude.

In order to determine the aerosol optical thickness and aerosol size distribution, a series of solar radiation measurements from Mauna Loa Observatory was collected (DeLuisi et al., 1982). The monthly mean stratospheric aerosol optical depths were determined from these data for June and July by subtracting the molecular scattering, ozone absorption and background tropospheric aerosol contributions from the total optical depth. These results, presented in the left portion of Fig. 3.1, show that the stratospheric aerosol layer resulting from the El Chichón eruptions had an optical depth between 0.15 and 0.25 throughout the visible wavelength region. This is more than an order of magnitude larger than background levels at Mauna Loa (Shaw, 1979) and larger than all but a small percentage of days at Tucson (King et al., 1980).

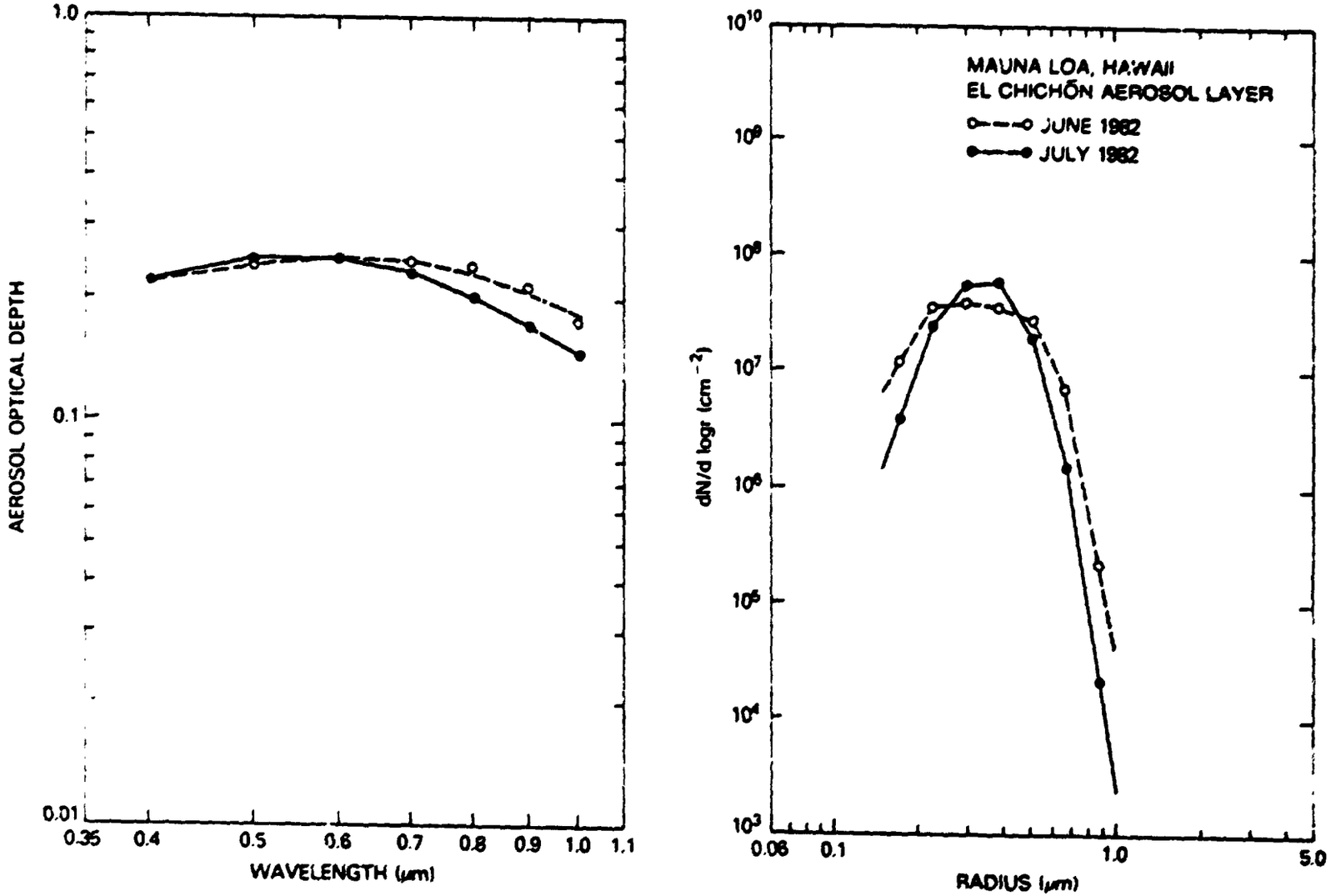

Figure 3.1. Monthly mean aerosol optical depths and estimated size distributions for measurements collected at Mauna Loa Observatory during June and July 1982. The curves on the left indicate the regression fit to the data using the inverted size distributions.

The columnar aerosol size distribution can be determined from the spectral variation of the aerosol optical depth using constrained linear inversion methods (King et al., 1978; King, 1982). The size distributions obtained by inverting the Mauna Loa measurements are presented in the right portion of Fig. 3.1, while the solid curves in the left portion indicate how the inverted size distributions are able to reproduce the aerosol optical thickness measurements. Due to the prominent negative curvature in the spectral optical thickness measurements, the corresponding size distributions are quite narrow with peak concentrations at radii between 0.3 and 0.4 μm. Though all inversions were performed assuming the complex refractive index of the aerosol particles was wavelength and size independent and given by m = 1.45-0.00i, it is well known that the refractive index sensitivity is quite weak, affecting the inverted size distribution slightly by shifting its magnitude and radii while maintaining its overall shape (King et al., 1978)

The columnar size distributions presented in Fig. 3.1 repres the number of particles per square cm per log radius interval in a vertical column through the stratosphere. For a particle density of 2 g cm^{-3}, the columnar mass loading for these cases is 0.0579 g m^{-2} and 0.0602 g m^{-2} for June and July, respectively. These mass loadings were obtained over the radii range $0.1 \leq r \leq 4.0$ μm by extrapolating the inverted size distributions to smaller and larger radii.

Both the June and July size distributions are well described by a modified gamma distribution of the form

$$\frac{dN}{d\log r} = Cr^{\alpha} \exp(-br), \qquad (1)$$

where the mode radius $r_o = \alpha/b$. Each distribution presented in Fig. 3.1 was fit to Eq. (1) using an efficient gradient-expansion method from nonlinear least-squares theory (Bevington, 1969). For the June distribution the best-fit parameters were $C = 1.549 \times 10^{15}$, $\alpha = 8.26$, $b = 24.4$ μm^{-1}, $r_o = 0.338$ μm and for July $C = 9.897 \times 10^{19}$, $\alpha = 13.65$, $b = 39.3$ μm^{-1}, $r_o = 0.347$ μm.

In addition to the mass loading, the inverted size distributions can be used to determine the optical thickness and phase matrix elements as a function of scattering angle and wavelength. Assuming the aerosol particles to be composed of $H_2SO_4 \cdot bH_2O$ droplets having a 75% concentration by weight of sulfuric acid, we obtained the aerosol optical thickness, single scattering albedo and asymmetry factor for wavelengths between 0.25 and 25.0 μm. For these computations, presented in Figs. 3.2-3.4, we used the July size distribution presented in Fig. 3.1 together with the complex refractive indices tabulated by Palmer and Williams (1975). Similar computations were performed using the modified gamma distribution having the appropriate parameters for the July distribution, but the results were virtually identical to those presented in Figs. 3.2-3.4. The optical thickness and single scattering albedo are the most important parameters governing the radiative properties of the aerosol layer in the near and thermal infrared. With the values of the optical thickness and single scattering albedo from Figs. 3.2 and 3.3 for λ = 3.7, 10.8 and 12.0 μm, for example, the El Chichón layer would be expected to produce a –0.6K bias in the AVHRR derived sea surface temperature at night (–1.2K during the day). In the 11.0 μm window region the emissivity of the layer is nearly unity ($\epsilon = 1 - \omega_0$) but the optical thickness has a strong wavelength dependence in this region. At 3.7 μm the emissivity is less and the aerosol optical thickness is greater than at 11 μm.

To examine the phase matrix in further detail, we computed the phase function and degree of polarization of the aerosol particles composing the stratospheric layer for a wavelength λ = 0.7 μm. This phase function, illustrated in Fig. 3.5, has an asymmetry factor g = 0.768, a single scattering albedo ω_0 = 1.000, and a ratio of the volume extinction to volume back-scattering coefficients S = 73.3 sr. The latter parameter has been found to be especially useful in analyzing monostatic lidar observations (Spinhirne et al., 1980; Reagan et al., 1980). The degree of polarization, illustrated in Fig. 3.6, has an unusually large number of scattering angles at which the polarization is neutral.

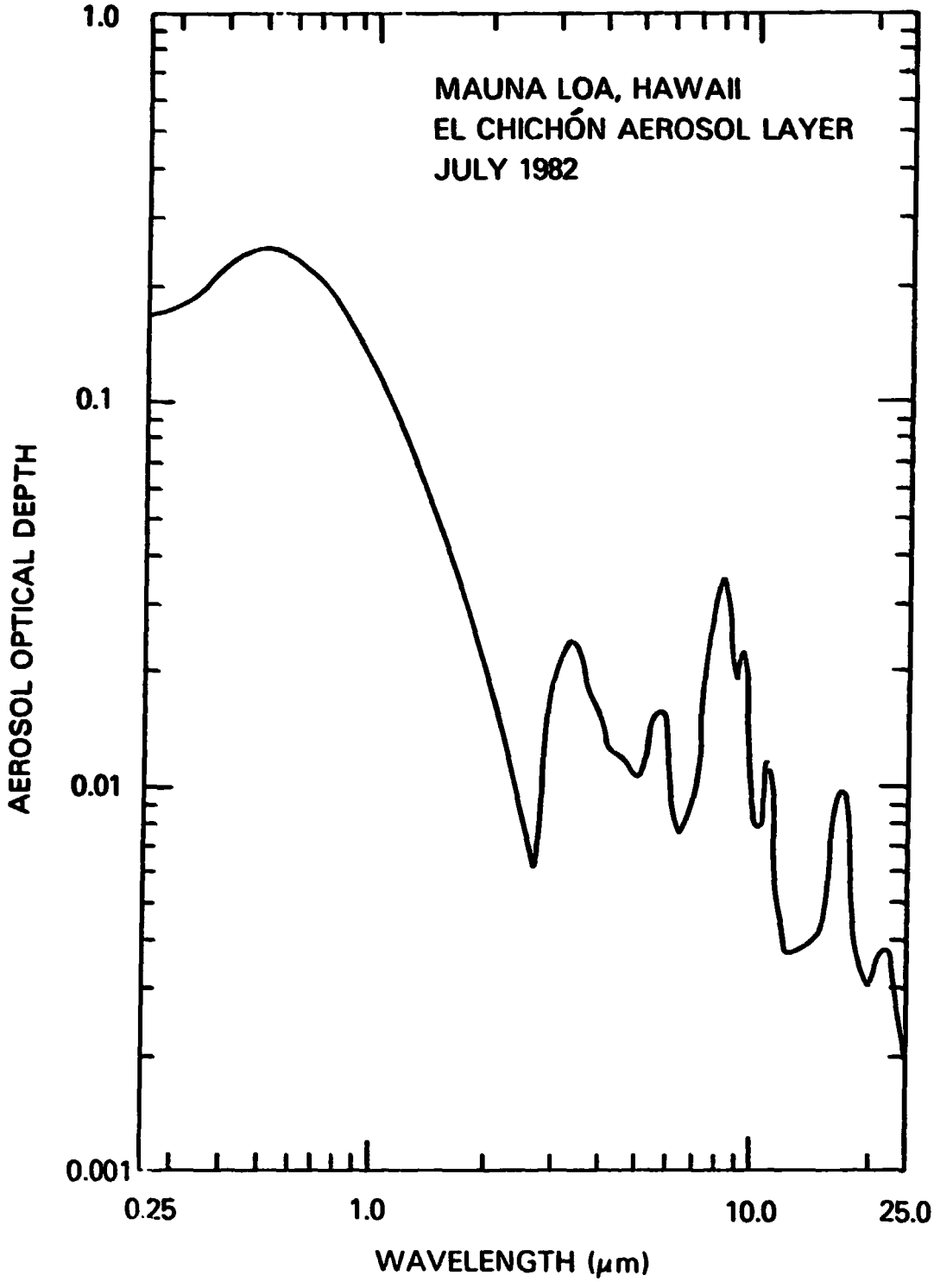

Figure 3.2. Aerosol optical thickness as a function of wavelength for the July 1982 stratospheric aerosol size distribution presented in Figure 3.1, where the aerosol particles are assumed to be composed of a 75% H_2SO_4 solution.

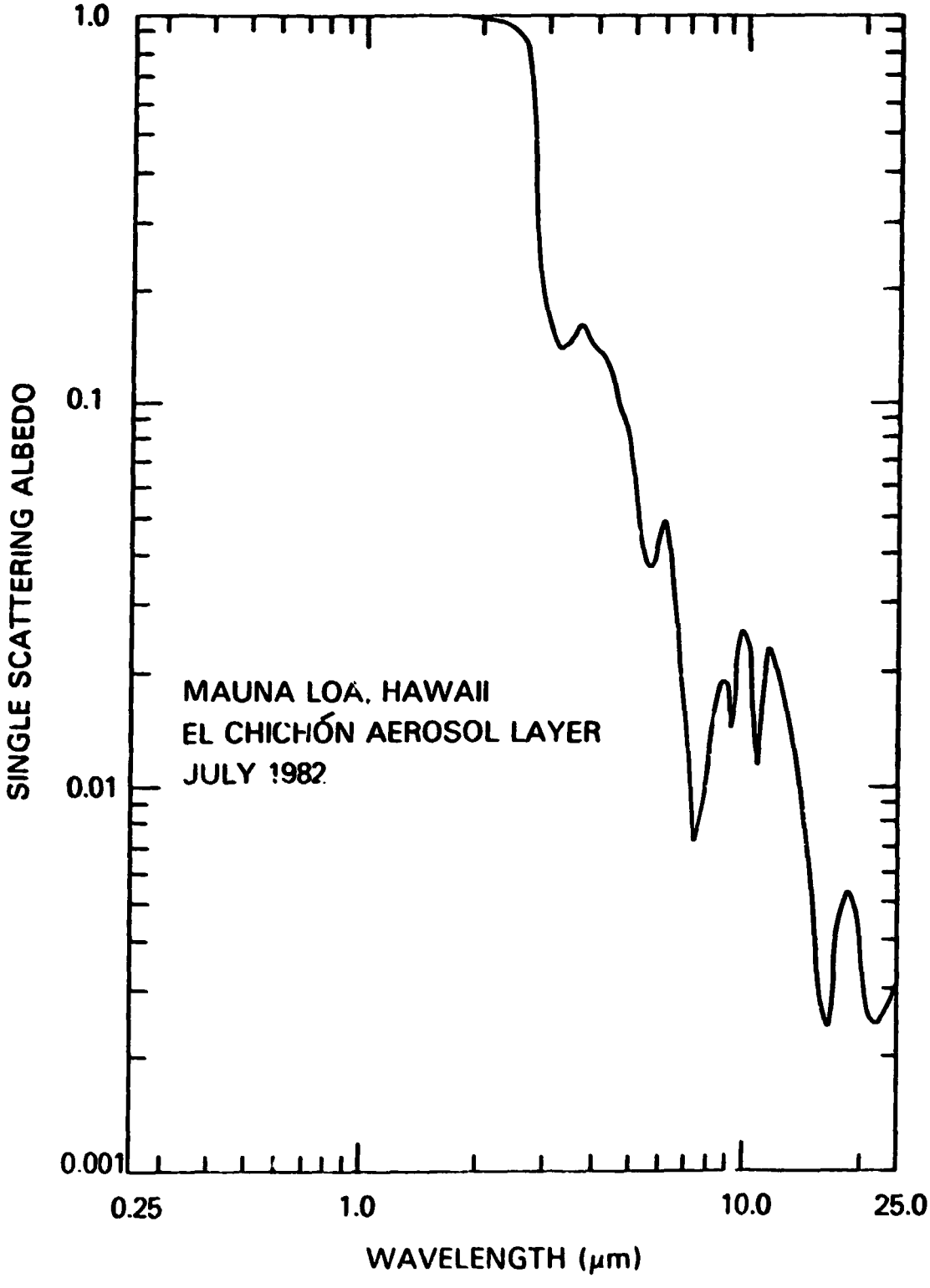

Figure 3.3. As in Figure 3.2 except for the single scattering albedo of the aerosol particles.

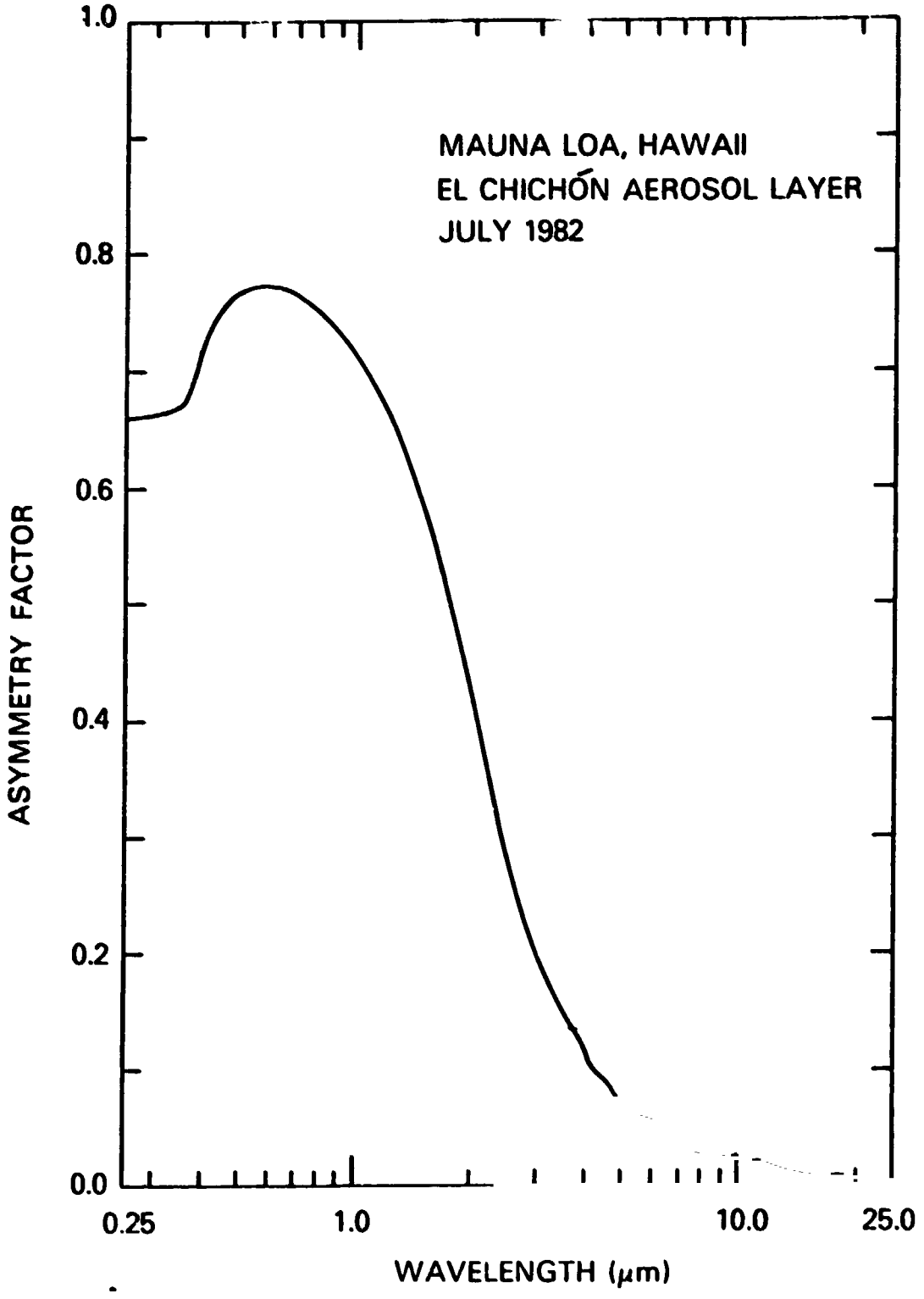

Figure 3.4. As in Figure 3.2 except for the asymmetry factor of the aerosol particles.

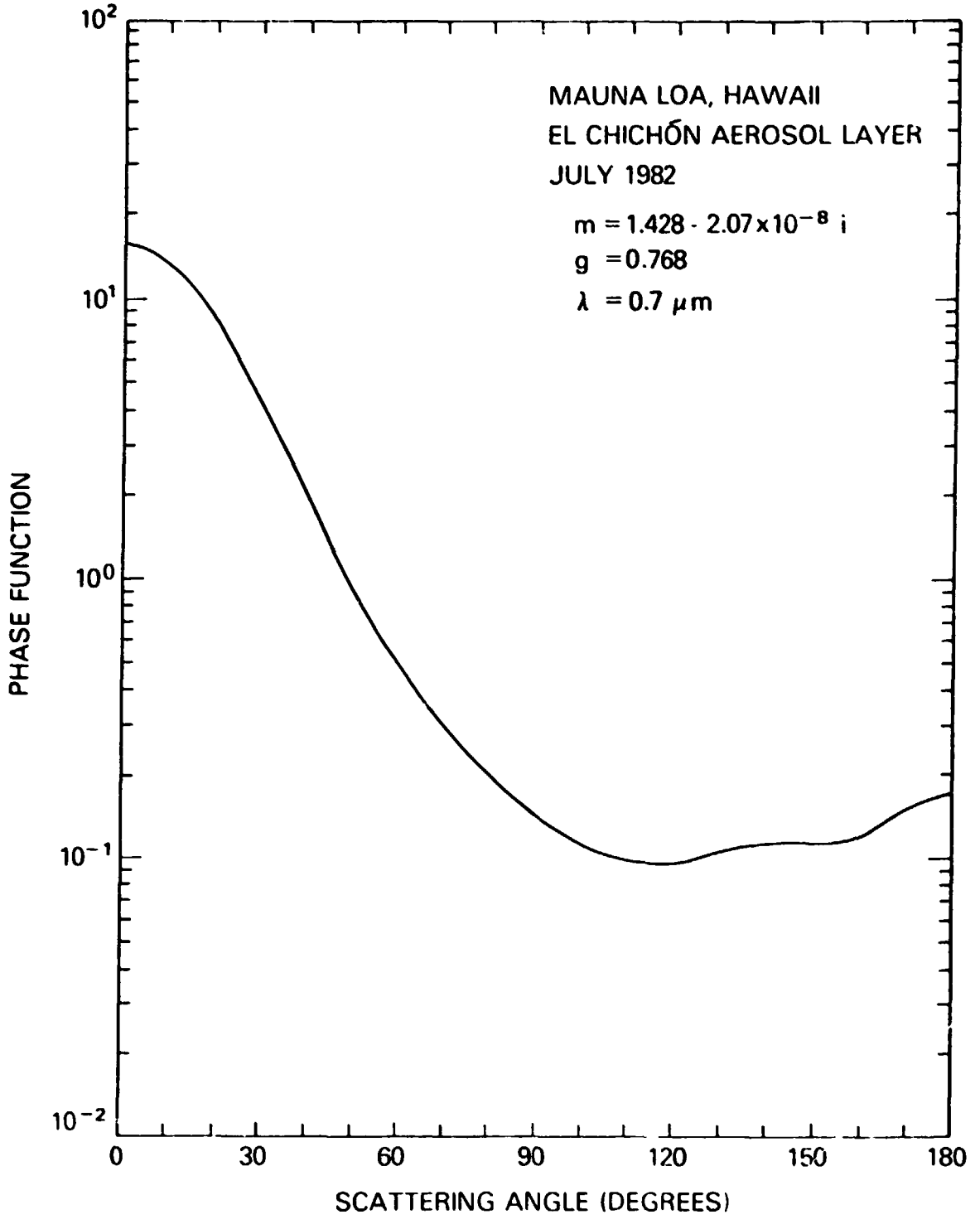

Figure 3.5. Phase function as a function of scattering angle for the July 1982 stratospheric aerosol size distribution presented in Figure 3.1, where $\lambda = 0.7\ \mu m$ and $m = 1.428 - 2.07 \times 10^{-8}i$. This phase function has an asymmetry factor $g = 0.768$ and an extinction to backscatter ratio $S = 73.3$ sr.

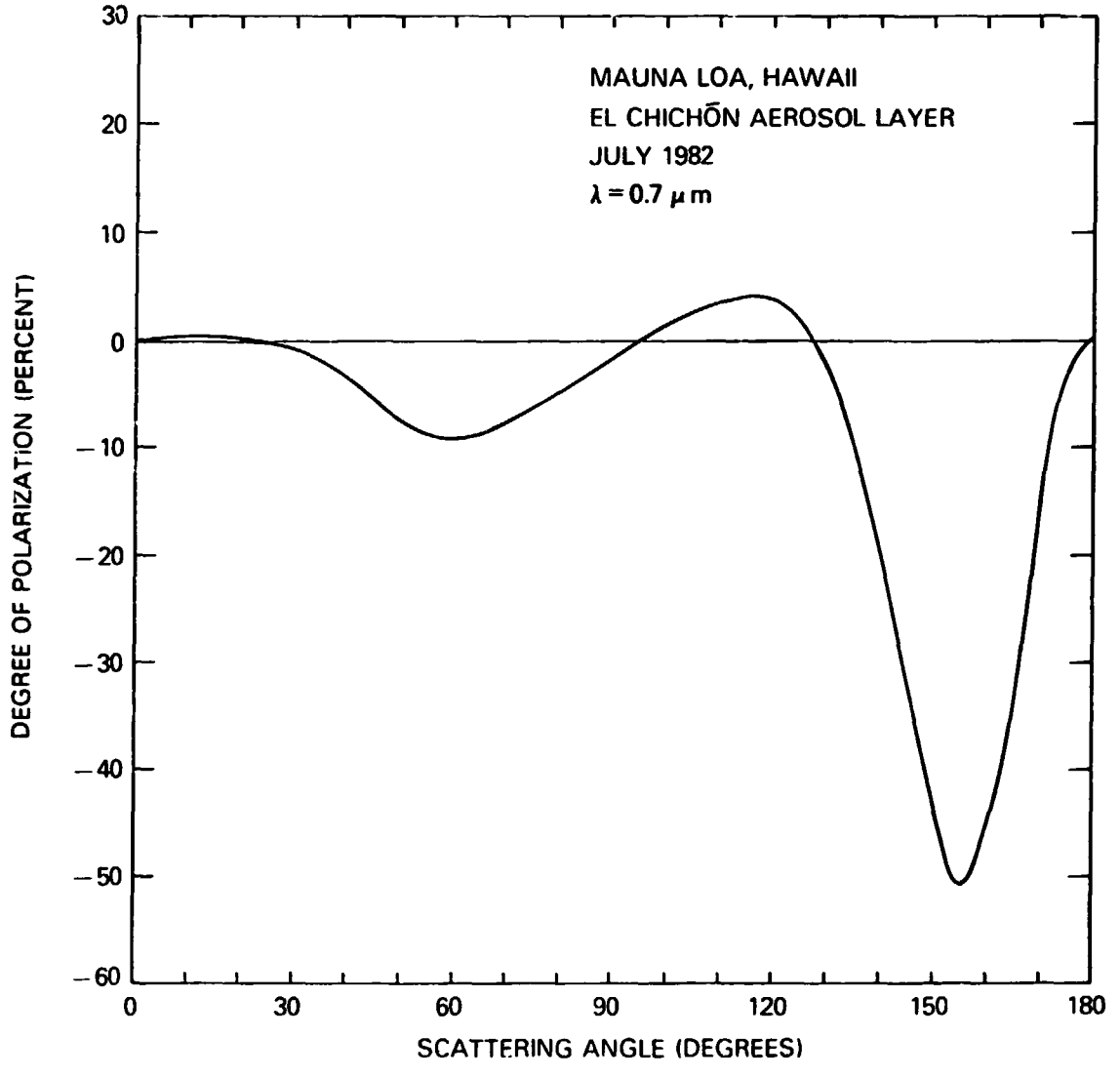

Figure 3.6. Degree of polarization $(I_r - I_\ell)/(I_r + I_\ell)$ as a function of scattering angle for incident unpolarized radiation and for the July 1982 stratospheric aerosol size distribution presented in Figure 3.1, where $\lambda = 0.7\ \mu m$ and $m = 1.428 - 2.07 \times 10^{-8} i$.

During the forthcoming months radiative transfer computations will be performed of the transmitted intensity and degree of polarization in the principal plane of the sun. These computations will initially be made using the optical thickness and phase matrix results presented in Figs. 3.1, 3.5 and 3.6 for July 1982 Mauna Loa observations. In addition, the vertical distribution of the aerosol particles obtained from monostatic lidar will be used. These computations will be compared with surface measurements collected by Coulson (1982) to validate our radiative transfer model and to verify that we understand the optical properties of the aerosol layer. Once satisfactory agreement has been achieved, the radiative transfer model will be used to examine the expected effects of the stratospheric aerosol layer on satellite observations. This research will be a collaborative effort between R. S. Fraser and M. D. King.

In addition to this investigation, a series of spectral optical thickness measurements between 0.44 and 0.87 μm have been collected by Dr. J. D. Spinhirne during a three week period in October and early November 1982. The solar transmission measurements were collected from NASA's Electra aircraft which flew from Wallops Island, VA to Santiago, Chile, and beyond. This flight covered the latitude range from 49°N to 46°S and data from the cloud-free daylight portion of the flight will be used to derive the latitudinal distribution of total ozone, aerosol optical thickness and aerosol size distribution.

M. D. King

References (Section 3.2)

Bevington, P. R., 1969: *Data Reduction and Error Analysis for the Physical Sciences.* McGraw-Hill, 336 pp.

Coulson, K. L., 1982: Effect of the volcanic cloud in the stratosphere on the polarization of light from the sky. Submitted to *Appl. Opt.*

DeLuisi, J., E. Dutton, B. Mendonca and M. King, 1982: Some radiative characteristics of the El Chichón dust cloud deduced from solar radiation measurements at Mauna Loa, Hawaii. Proc. AGU Fall Meeting, San Francisco, CA.

King, M. D., 1982: Sensitivity of constrained linear inversions to the selection of the Lagrange multiplier. *J. Atmos. Sci.*, 39, 1356-1369.

_____, D. M. Byrne, B. M. Herman and J. A. Reagan, 1978: Aerosol size distributions obtained by inversion of spectral optical depth measurements. *J. Atmos. Sci.*, 35, 2153-2167.

_____, _____, J. A. Reagan and B. M. Herman, 1980: Spectral variation of optical depth at Tucson, Arizona between August 1975 and December 1977. *J. Appl. Meteor.*, 19, 723-732.

Shaw, G. E., 1979: Aerosols at Mauna Loa: Optical properties. *J. Atmos. Sci.*, 36, 862-869.

Palmer, K. F., and D. Williams, 1975: Optical constants of sulfuric acid; Application to the clouds of Venus? *Appl. Opt.*, 14, 208-219.

Spinhirne, J. D., J. A. Reagan and B. M. Herman, 1980: Vertical distribution of aerosol extinction cross section and inference of aerosol imaginary index in the troposphere by lidar technique. *J. Appl. Meteor.*, 19, 426-438.

Reagan, J. A., D. M. Byrne, M. D. King, J. D. Spinhirne and B. M. Herman, 1980: Determination of the complex refractive index and size distribution of atmospheric particulates from bistatic-monostatic lidar and solar radiometer measurements. *J. Geophys. Res.*, 85, 1591-1599.

4. EFFECTS OF EL CHICHON ERUPTIONS ON SATELLITE OBSERVATIONS

4.1. NOAA/AVHRR PRODUCTS

4.1.1. Change in albedo

Satellite measurements of planetary radiation from NOAA-7 AVHRR data have been scrutinized to examine the impact of El Chichón. It was known in May 1982 that an overall increase in albedo was produced because the number of daytime satellite retrievals of sea surface temperature (SST) (see below) had decreased markedly in the latitude band affected by El Chichón. This decrease has been shown to be due almost entirely to a test using a threshold for reflected radiation. This test does not accept any SST retrievals unless the albedo in AVHRR channel 2 (λ 0.71-0.99 μm) falls below 1.7%. This albedo is referenced to the response that would occur by the AVHRR observing a Lambert surface with 100% albedo, when exposed to the solar radiant energy above the atmosphere.

Albedo data from the NESDIS operational planetary radiation budget archive have been examined using a 10-day minimum albedo classification. Minimum daily albedos at every 2.5° lat/long grid were retained globally over each 10-day period. A composite minimum albedo was constructed every month (3-ten day periods) using a simple arithmetic mean of all three values at each grid location. These may be contrasted with a similar sequence in 1979. The albedos for the areas of minimum cloudiness between 0° to 30°N are greater in 1982 than in 1979. This anomaly was still persisting during September 1982.

Four target areas within this aerosol belt were selected for further examination. Measurement of albedo in cloud-free areas was noted immediately prior to the passage of the dust cloud (see section 2.1) and just after dust cloud passage. In this table the albedo was corrected for the cosine of the solar zenith angle. Cloud-free scenes were examined further for daytime outgoing longwave radiation. The results are shown in Table 4.1. Albedos over the cloud-free ocean have nearly doubled, from about 5% to 10%, while outgoing flux shows a several watt/m^2 decrease.

Table 4.1
Cloud-Free Radiation Changes for Four Areas: Eastern Pacific (10-20N, 10[illegible]15W); Philippine Sea (10-20N, 125-135E); Bay of Bengal (5-15N, 85-95E); and Arabian Sea (10-20N, 60-70E).

	Albedo (%)	Increase (%)	Outgoing Long Wave (11-12 μm; WM^{-2})	Decrease (WM^{-2})
Eastern Pacific				
2 April	5.1		304	
6 April	10.4	5.3	294	10
Philippine Sea				
14 April	6.0		299	
15 April	7.3	1.3	296	3
Bay of Bengal				
6 April	4.5		305	
18 April	10.5	6.0	291	14
Arabian Sea				
15 April	4.3		303	
19 April	10.6	6.3	296	7

4.1.2. Sea surface temperature

As mentioned above, AVHRR processing for multichannel sea surface temperature (MCSST) initially responded to the El Chichón eruptions with a drastic reduction in daytime retrievals and a pronounced negative bias (temperature lower than those from ships) on those nighttime observations that passed all cloud tests. Drifting buoy validation statistics had been showing ±0.5°C accuracies (RMSD) before the eruption and continue to show similar [±0.5°C] accuracies outside the contaminated belt. Initial biasing was seen at fixed buoy matchup positions within the aerosol cloud at locations such as Hawaii and in the Gulf of Mexico. One such example is given in Fig. 4.1 using differences from a large moored NOAA buoy (#42003) in the central Gulf of Mexico. The final eruption on 4 April (Julian Day 94) marks the start of a −1.5°C bias that remained virtually constant until 25 J[illegible] when apparently another level of aerosol moved north over the buoy location causing

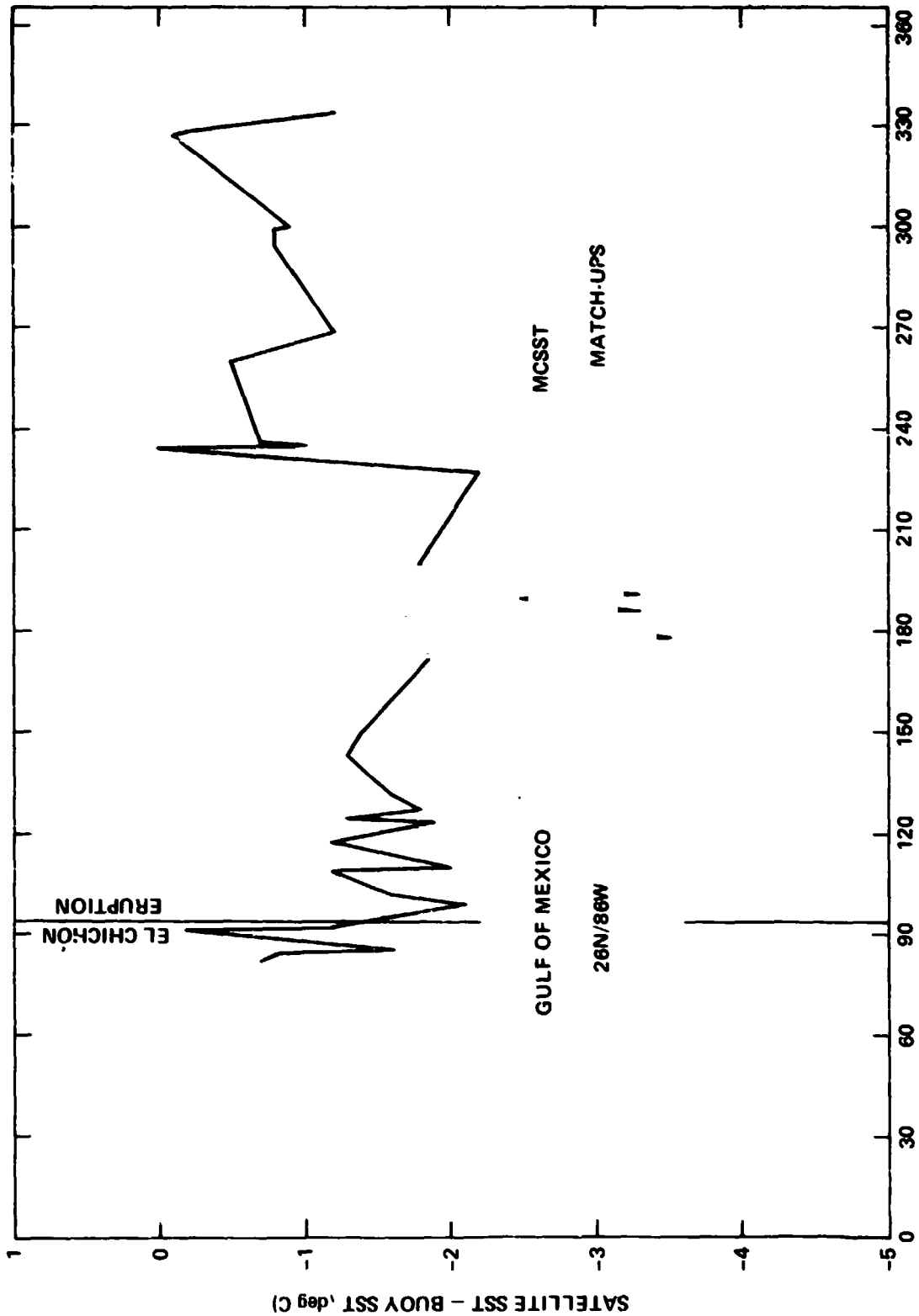

Figure 4.1. Difference (bias) of satellite MCSST and NOAA fixed buoy (#42003) in the Gulf of Mexico (26N, 86W) during a portion of 1982.

a greater than –2°C offset in derived MCSST from AVHRR. The absolute value of the bias decreased after the summer by 2°C, perhaps as a result of the stratospheric aerosol layer thinning out.

The final series of Fig. 4.2a-e shows the apparent extent of the volcanic cloud on a monthly mean basis using this negative bias relative to ships as an indicator of aerosol intensity. Monthly mean data were differenced using ship and buoy only and satellite only. Areas exhibiting differences exceeding 1C have been highlighted thereby revealing spread and diffusion of the cloud throughout the summer.

The following observations can be made:

1. Maximum contamination occurred during July, probably when SO_2 conversion to H_2SO_4 was nearly complete and before the larger particles had fallen out of the stratosphere.

2. Some transport north of 30N has been observed on a monthly basis, especially over the central Pacific, but most of the aerosol continues to occupy the latitudinal belt of 0 to 30N.

3. Evidence of movement into the Southern Hemisphere to 10S has been observed since June, particularly over the South Equatorial Atlantic Ocean. (The paucity of ship observations may be responsible for holding back any spread of negative bias in the MCSSTs in the central and eastern South Equatorial Pacific.)

4. Beginning in August the area around Indonesia became incorporated into the El Chichón belt. It is possible that the June-August eruptions of Galunggung were responsible for this.

5. During September an apparent migration of aerosol northward over Japan has been noted. Since August, lidar observations from Fukuoka, Japan have been showing more aerosol, particularly at 20-23 km (below El Chichón's 25-30 km altitude), that may be moving northward from Galunggung in Indonesia.

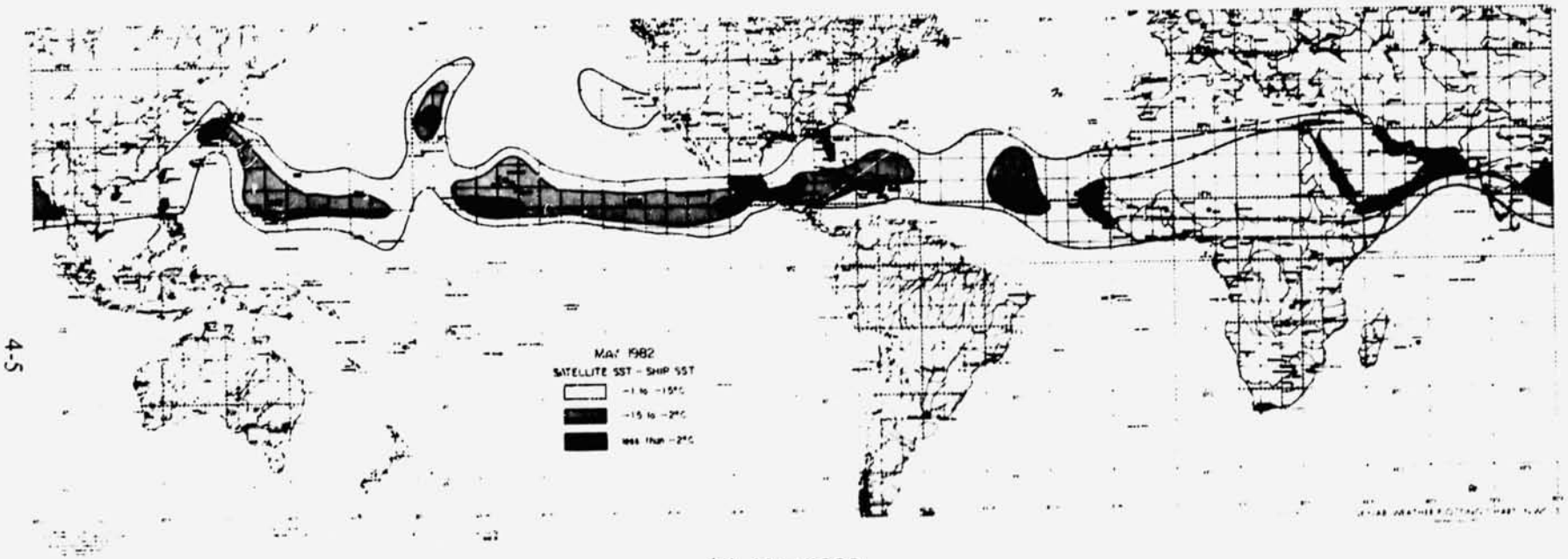

(a) May 1982

Figure 4.2. Negative bias distribution of monthly mean satellite MCSST from ship SST for (a) May 1982, (b) June 1982, (c) July 1982, (d) August 1982, (e) September 1982. Good correspondence has been seen between regions of negative bias and El Chichón aerosol, as observed from ground and aircraft based lidar systen

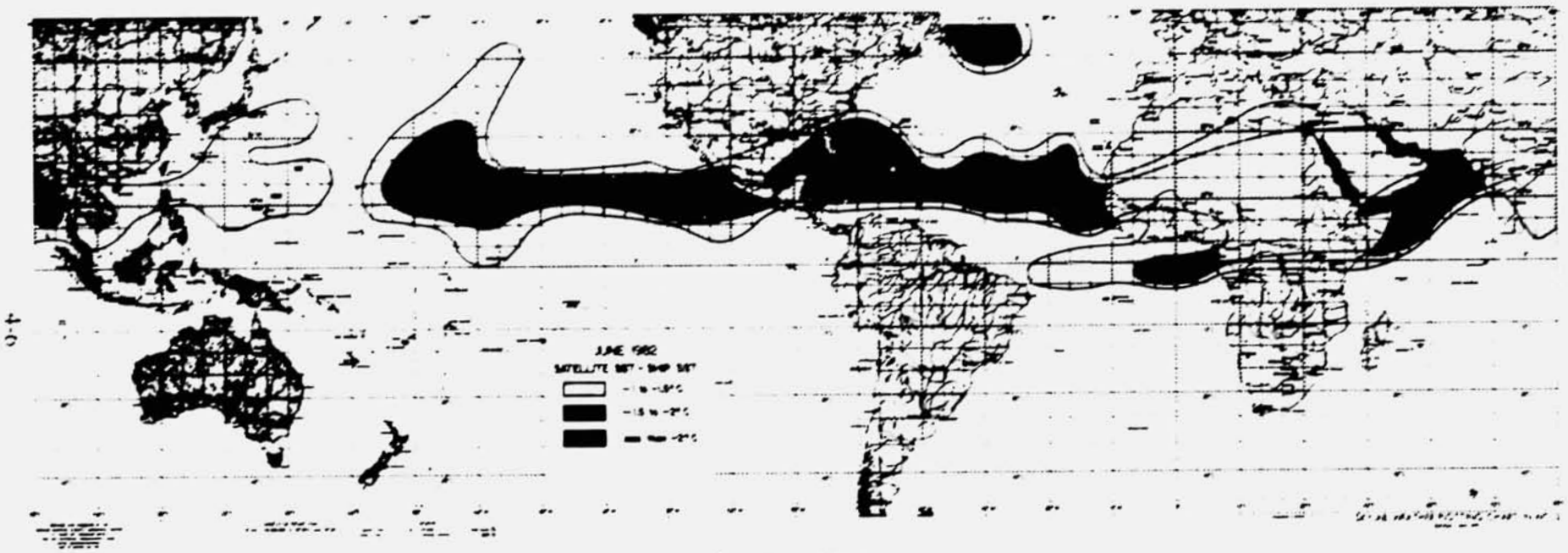

(b) June 1982

Figure 4.2. (Continued)

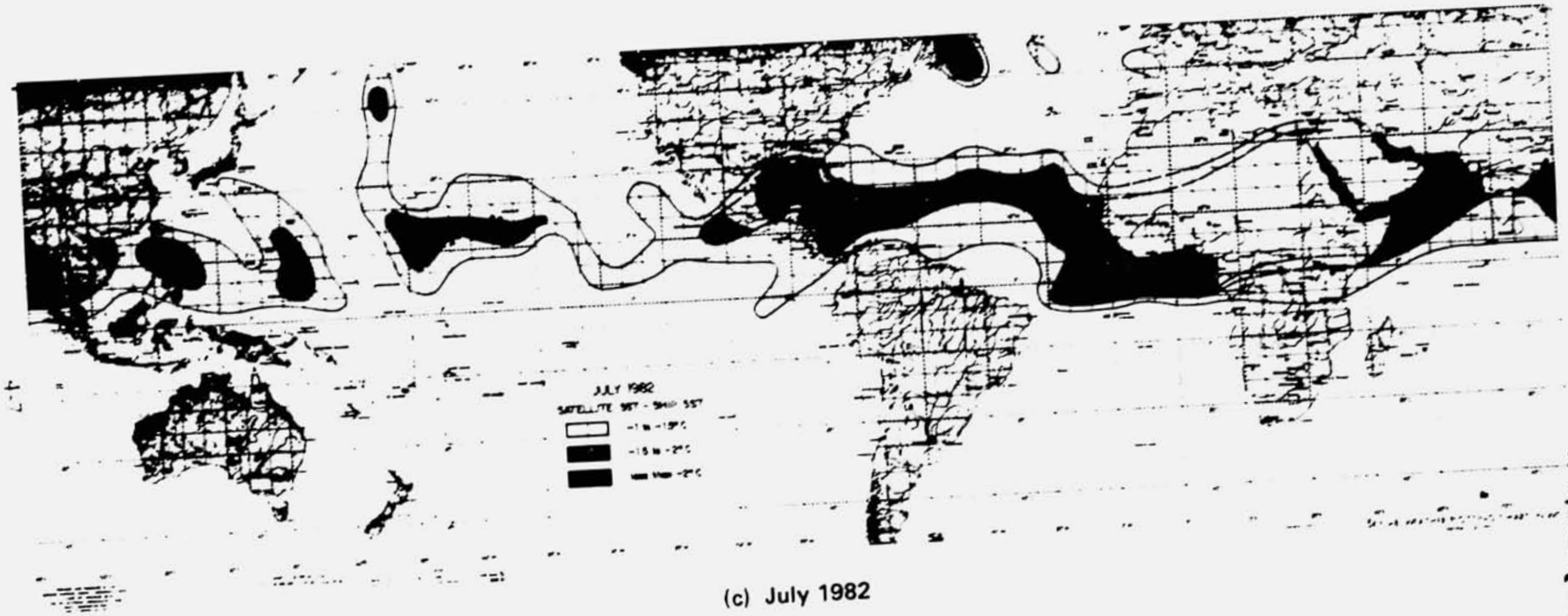

(c) July 1982

Figure 4.2. (Continued)

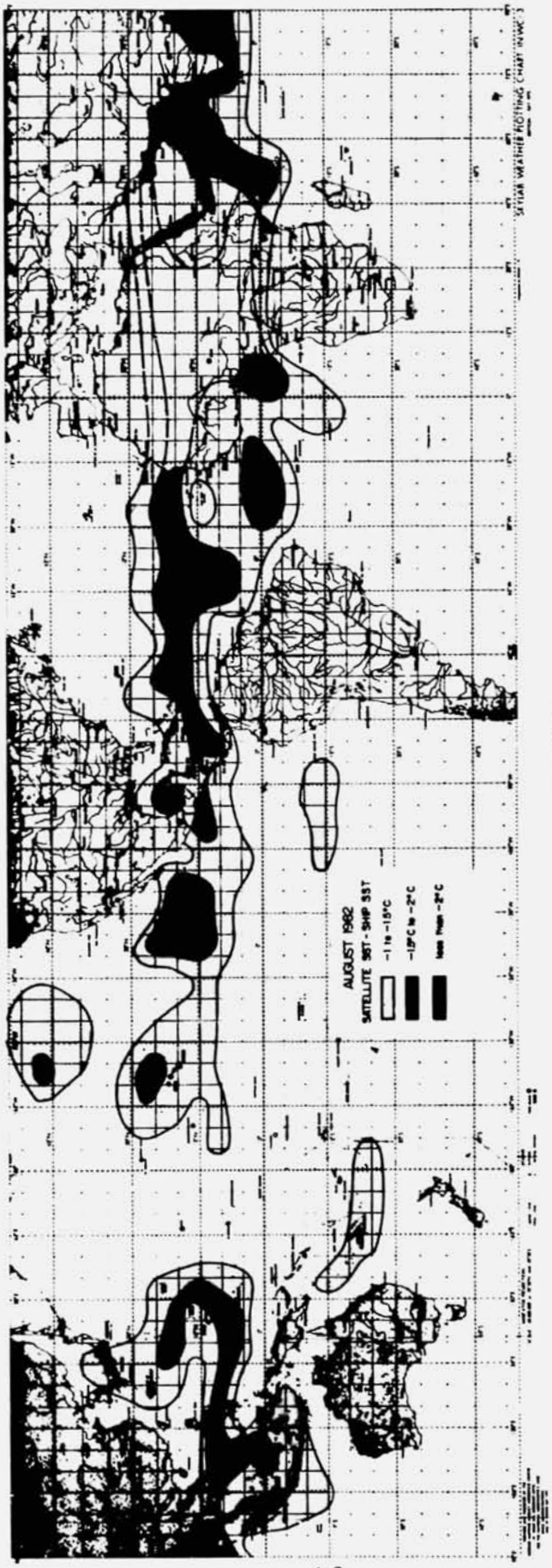

(d) August 1982

Figure 4.2. (Continued)

(e) September 1982

Figure 4.2. (Continued)

6. By September the general levels of bias exhibited by the satellite-derived MCSSTs appear to have lessened over the Western Hemisphere, although the distribution has remained largely unchanged since July and August. Lower levels are presumed to be attributed to fallout of larger particles from the stratosphere, which emit radiation at lower temperatures.

The negative bias in the MCSST sea surface temperature decreases after the 230 day (Fig. 4.1). Perhaps this change results from smaller (<1 micron) particles remaining after the larger ones (>1 micron) fall out into the troposphere. We are investigating several aerosol correction schemes at NESDIS for incorporation into the MCSST procedures. If successful, this would provide a means for continuous monitoring of aerosol, as well as providing a mechanism to remove subsequent volcanic contamination effects on the retrieval of sea surface temperatures from satellite infrared measurements.

4.1.3. Aerosol remote sensing

An algorithm has been developed and tested in ground-truth experiments to convert the radiance measured by AVHRR Channel 1 (0.56-0.68 μm) over cloudless ocean areas into an aerosol optical thickness at a wavelength of 0.5 μm (Griggs, 1981). A table look-up procedure is used. The table was constructed using the multiple scattering code of Dave for a plane parallel atmosphere with Lambertian Earth surface reflectance. The parameters of the model were chosen to give agreement between theory and observation using Landsat 1 MSS data and Volz type sun-photometer solar extinction measurements off the coast of San Diego. Figure 4.3a shows a comparison of the optical thickness derived from this algorithm applied to NOAA-6 AVHRR Ch 1 data and sun-photometer extinction measurements at several locations used in a 1980 groundtruth experiment. One N unit is equivalent to an aerosol optical thickness of 0.213 at λ 0.5 μm. The two estimates are in good agreement. The correlation coefficient is 0.93 and the standard error about a linear regression line is ±0.25N (±0.05 in optical thickness).

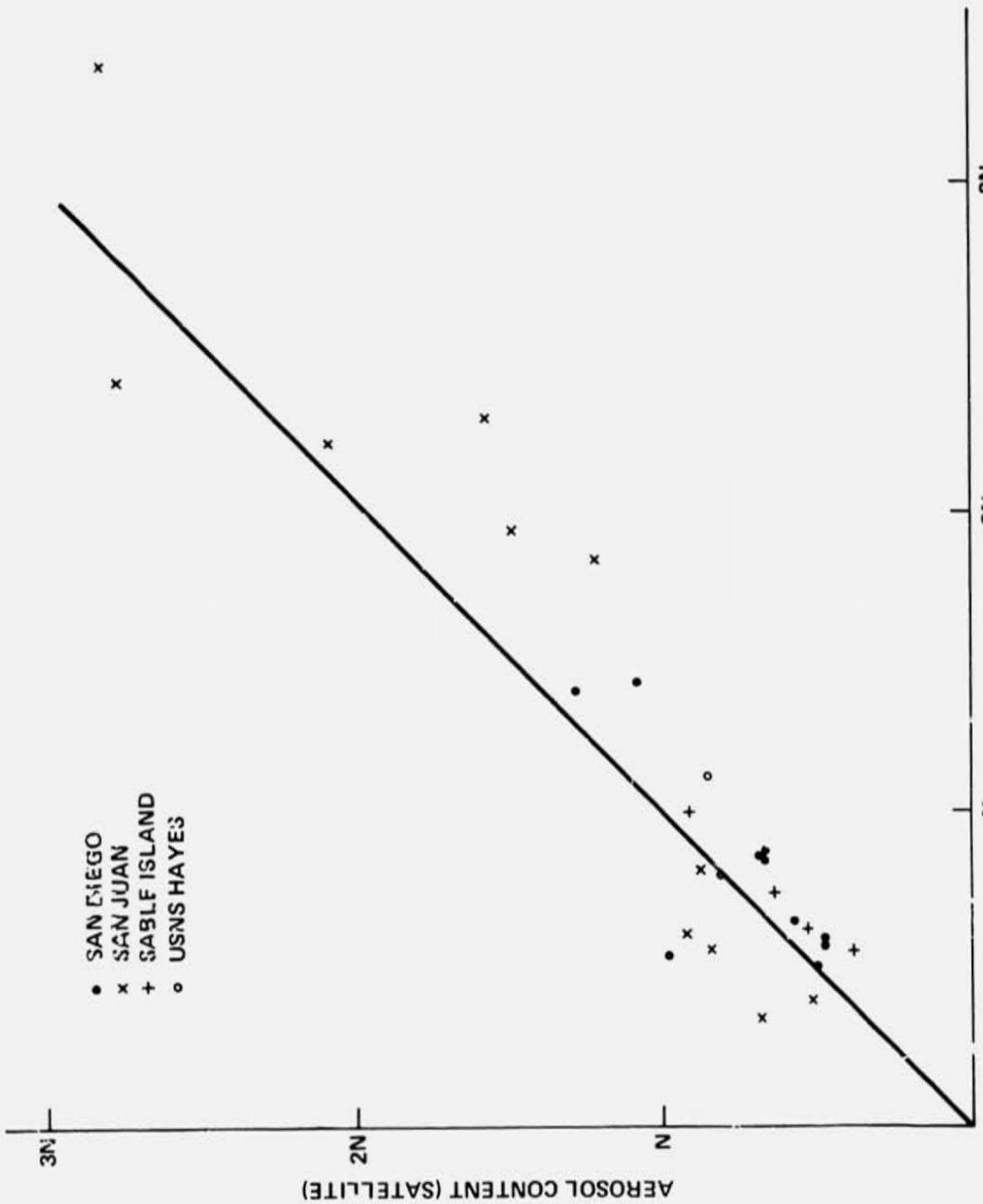

Figure 4.3a. Comparison of AVHRR and ground truth measurements of aerosol content, when the solar zenith angle is less than 70°.

Figure 4.3b shows a comparison between aerosol optical thickness derived from NOAA-7 AVHRR data and from sun-photometer data at the Mauna Loa observatory between March 29, 1982 and April 28, 1982. The aerosol was first observed at Mauna Loa on April 9th. The area being studied with AVHRR data is about 800 km WNW of Mauna Loa, so the aerosol probably arrived in this area on the 11th. However, due to constraints imposed by clouds or sun-glint effects, the first possible AVHRR aerosol measurement occurred on the 16th. Since this area is quite distant from Mauna Loa and the AVHRR measures total optical depth to the sea surface, whereas the Mauna observations are made 3.4 km above the sea, the observations are in very good agreement. Of particular interest is the decrease in optical depth after the 18th at both locations, suggesting that the aerosol cloud had both a leading and trailing edge. The numbers next to the AVHRR points represent the number of water cloud screening tests passed out of a total of eight. These tests are used in the MCSST program and indicate that the aerosol cloud is being classified as a water cloud by many of these tests; hence, no surface temperatures would be derived on these dates.

A method is currently underdevelopment which uses Ch 1 and Ch 2 AVHRR data. Preliminary results suggest that information on aerosol size distribution as well as optical thickness can be extracted from a two channel algorithm.

A. E. Strong
A. Gruber
L. Stowe

References (Section 4.1)

Griggs, M., 1981: AVHRR measurements of atmospheric aerosols over oceans. Contract Report, NOAA MO-A01-78-00-4092, Nov. 18, 1981, 50 p.

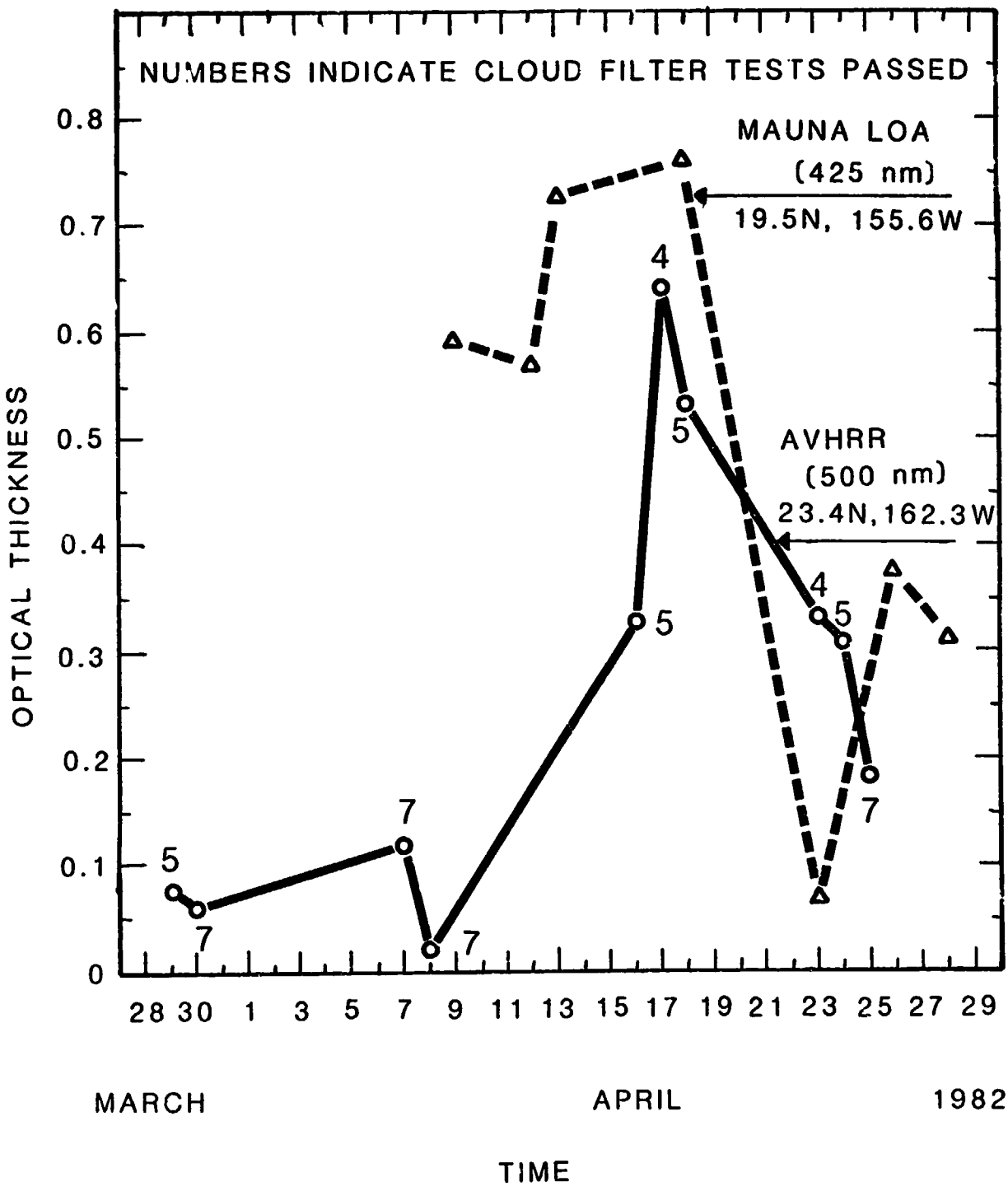

Figure 4.3b. El Chichón aerosol optical thickness versus time.

4.2 HIRS/MSU SOUNDERS

4.2.1. Background

HIRS and MSU are components of the operational infrared and microwave temperature and humidity sounders on the satellites NOAA-6 and NOAA-7. Table 4.2 shows the central frequency (ν) for each channel; the third column gives the pressure p at the peak of the weighting function, $d\tau/d\ln p$, for each of the temperature sounding channels; τ is the vertical transmission of the atmosphere. The pressure corresponds to the level of the atmosphere where the typical atmospheric optical depth is one above that level. The fourth column gives the pressure level at the peak of the product of the weighting function and the Planck black body function (B) of the atmospheric temperature (T). This product, after being normalized to the total radiance (I) at the top atmosphere, is plotted along the abscissa as a function of pressure for the HIRS and MSU channels in Figs. 4.4-4.6. The HIRS observations have a horizontal resolution of 18 km at nadir, changing to 60 km at a 55° angle from the nadir. Under the same conditions, the MSU resolution changes from 100 km to 300 km.

Global atmospheric temperature retrievals are produced operationally from the HIRS2/MSU data. In addition, NASA has developed a research oriented processing system for the HIRS2/MSU data (Susskind et al., 1982) which deduces not only atmospheric temperature profiles but also sea surface temperature, ice and snow cover, and percent cloud cover and cloud height from this data. Two distinct questions are of interest. The first question is the extent, if any, that the quality of

Table 4.2
HIRS2 and MSU Channels

Channel	ν (cm^{-1})	Peak of $d\tau/d\ln p$ (mb)	Peak of $Bd\tau/d\ln p$ (mb)
H1	668.40	30	20
H2	679.20	60	50
H3	691.10	100	100
H4	703.60	280	360
H5	716.10	475	575
H6	732.40	725	875
H7	748.30	Surface	Surface
H8	897.70	Window, sensitive to water vapor	
H9	1027.90	Window, sensitive to O_3	
H10	1217.10	Lower tropospheric water vapor	
H11	1363.70	Middle tropospheric water vapor	
H12	1484.40	Upper tropospheric water vapor	
H13	2190.40	Surface	Surface
H14	2212.60	650	Surface
H15	2240.10	340	675
H16	2276.30	170	425
H17	2310.70	15	2
H18	2512.00	Window, sensitive to solar radiation	
H19	2671.80	Window, sensitive to solar radiation	
M1	50.30a	Window, sensitive to surface emissivity	
M2	53.74a	500	
M3	54.96a	300	
M4	57.95a	70	

a values in GHz

the retrieved products is degraded as a result of the volcano. The second question is the extent to which sounding data can give us additional information about the volcanic eruption and its radiative effects.

Thus far, the byproducts of El Chichón eruption have been observed indirectly, as degraded products of ozone and sea surface temperature from analyses of TOMS and AVHRR data, and directly, from the visible imagery of AVHRR. It is thought that TOMS is observing primarily the effects of SO_2 gas from the eruption and AVHRR is being affected by aerosols.

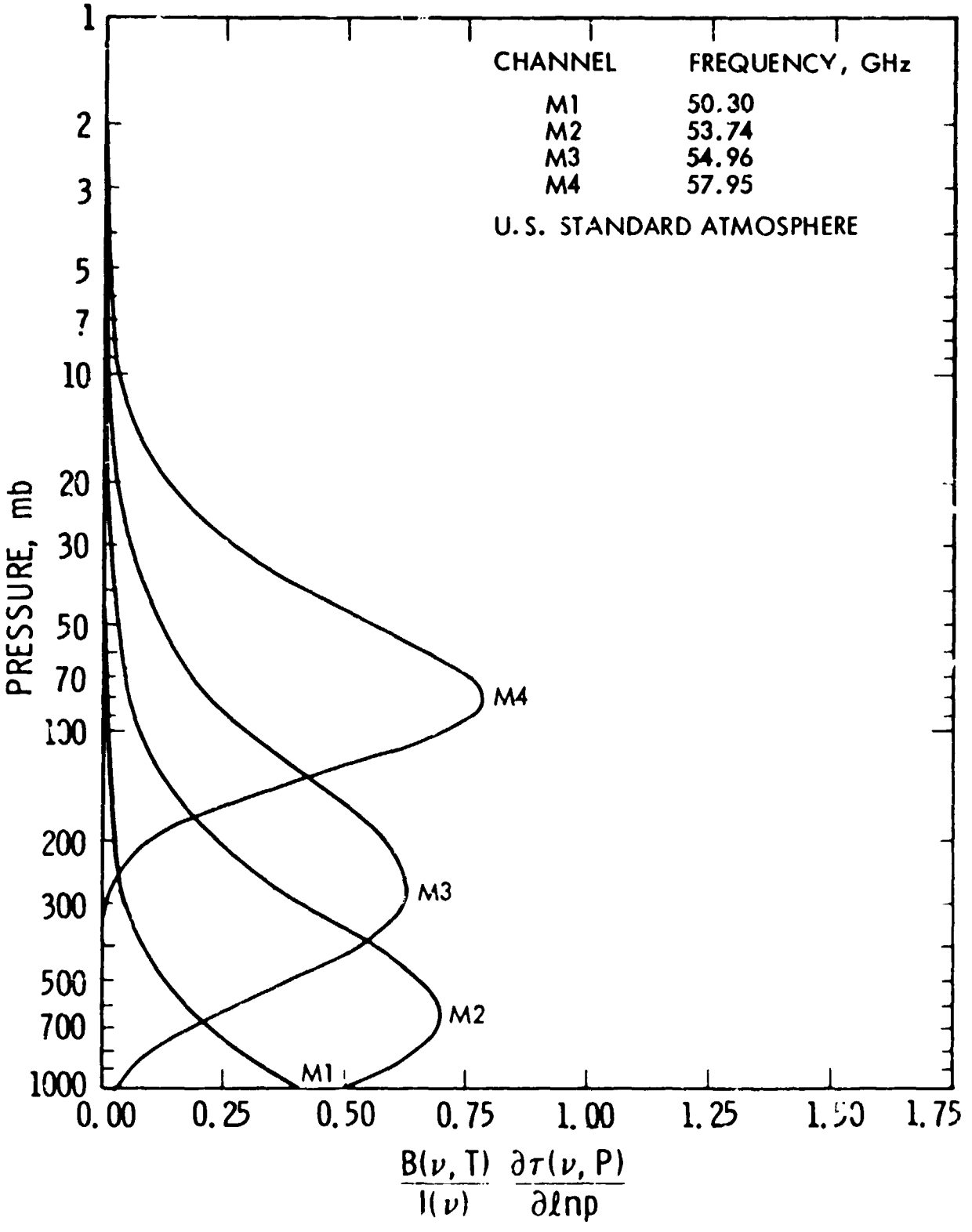

Figure 4.4. Normalized source function for the MSU temperature sounding channels.

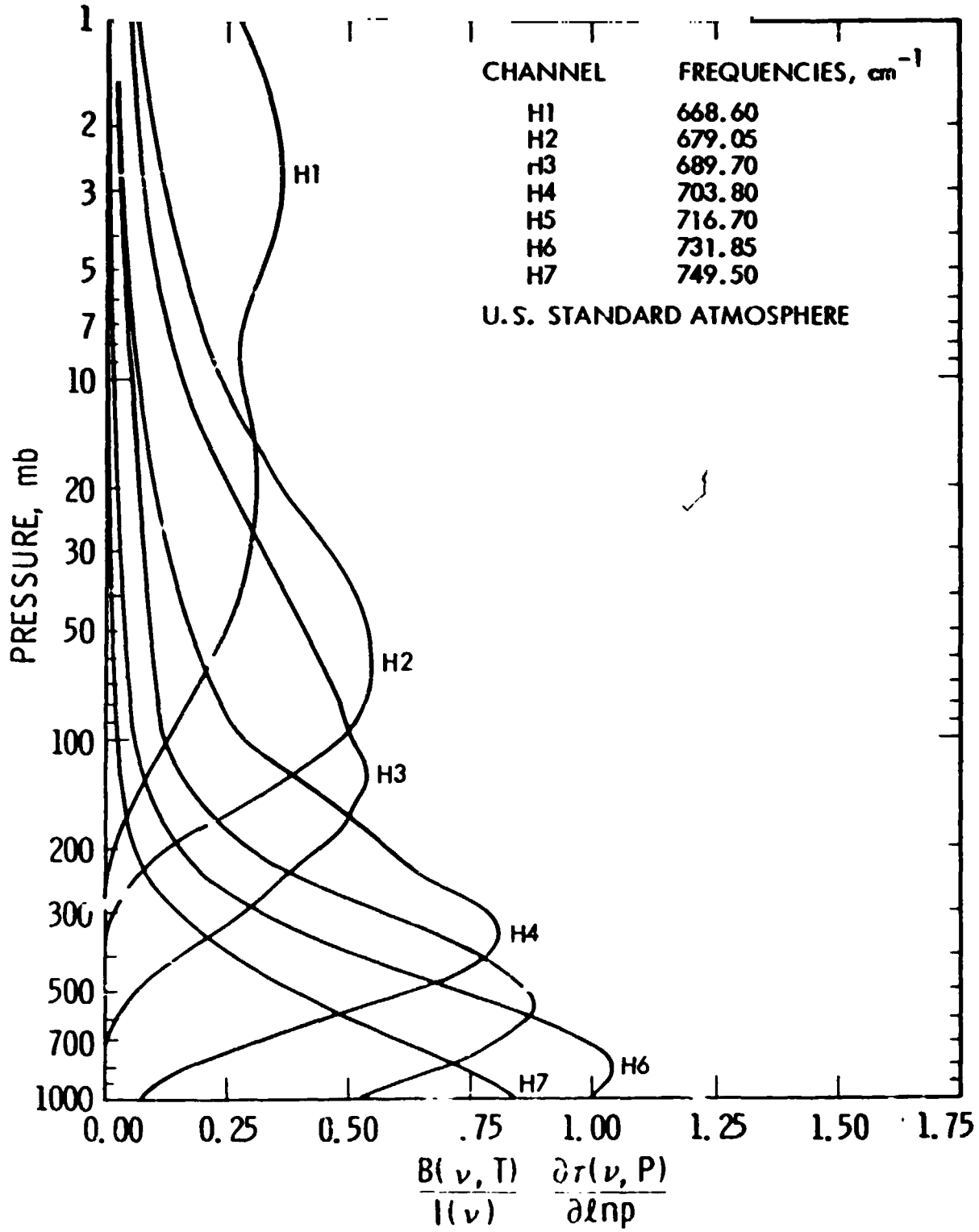

Figure 4.5. Normalized source function for the HIRS 15 μm temperature sounding channels.

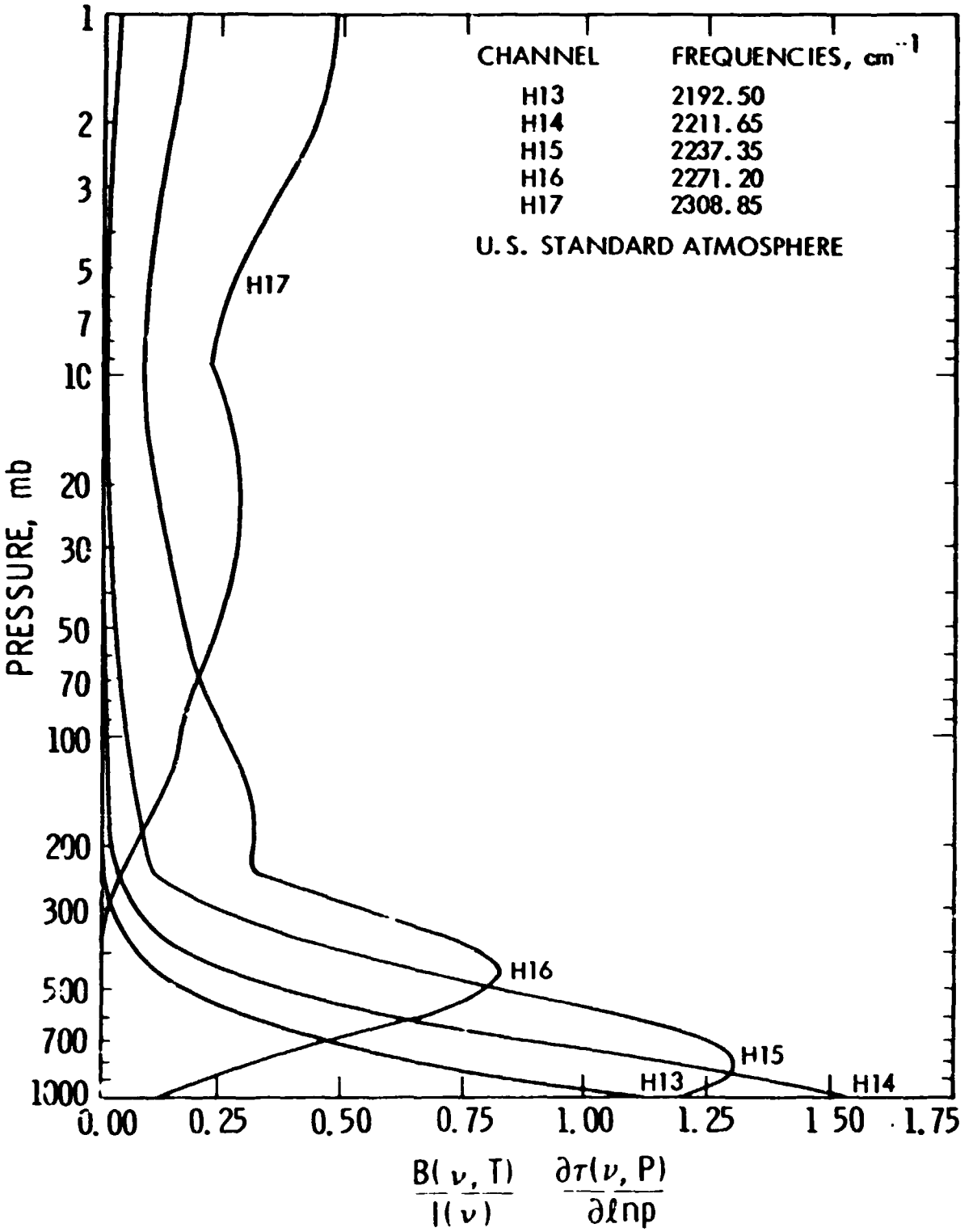

Figure 4.6. Normalized source function for the HIRS 4.3 μm temperature sounding channels.

While SO_2 affects observations in the channels of TOMS, SO_2 has no appreciable absorption in any of the channels of AVHRR or the temperature sounding channels of HIRS. Therefore, one would not expect it to degrade the retrieved temperature fields in any way. SO_2 does absorb, to some extent, in HIRS channels 11, 10 and 18 in decreasing order of strength. The first two channels are primarily for humidity sounding. The retrieved humidities may therefore be affected. The last channel, 18, is a shortwave window channel used by GLAS to obtain sea surface temperature. During the day, channels 18 and 19 are used together to solve simultaneously for the surface temperature and the bi-directional reflectance of solar radiation. At night, independent estimates of surface temperatures can be obtained from the radiances of each channel (18 or 19). In general, these estimates differ by less than 1°C. The difference in sea surface temperature retrieved from these two channels can serve as a tracer for SO_2. The effect is expected to be very small however.

The H_2SO_4 aerosol is expected to have broad banded attenuation features throughout the 3-15 μm regions sampled by the HIRS and AVHRR instruments. This attenuation is due almost exclusively to absorption, as shown in Fig. 3.2 and 3.3. Channels 3 (3.55-3.93 μm) and 4 (10.5-11.5 μm) on AVHRR both contain frequencies characterized by relatively large H_2SO_4 absorption and the effect of this absorption has been noted on the sea surface temperature fields retrieved from AVHRR, utilizing these channels. Sea surface temperatures from HIRS2 are retrieved by GLAS primarily from the two shortwave window channels 18 (3.95-4.00 μm) and 19 (3.71-3.83 μm) which have considerably less absorption due to H_2SO_4 aerosol than AVHRR channel 3. The longwave window channel 8 (10.9-11.3 μm) has comparable absorption to that of AVHRR channel 4 but this channel is not used by GLAS to retrieve sea-surface temperature.

It can be inferred from Kornfield and Susskind (1977) that the brightness temperature in a window channel at frequency $\nu(cm^{-1})$ will differ from the surface temperature T_S by approximately

$$\Delta T = \frac{T_S^2(1-\tau)}{1.439\nu} \qquad (1)$$

if the radiation is weakly attenuated. This implies that absorption at 11 μm is three times more effective than the same absorption at 3.7 μm in depressing the brightness temperatures. From Fig. 3.2, one would expect a brightness temperature error of about 0.8°C at 11 μm at nadir and 300°K surface temperature, and likewise about 0.8°C in AVHRR channel 3 at about 3.7 μm. This error is magnified in the analysis of the operational AVHRR data because of the use of regression. In HIRS channels 18 and 19, however, the error is expected to be much smaller and potentially insignificant. In addition, in the physical retrieval method, no regression is used and an error in computed brightness temperature results in the same error in sea-surface temperature.

An obvious after effect of the volcanic eruption is the visible cloud tracked around the globe by Matson (see section 2.1). This same cloud is readily apparent in most IR channels. By observing this cloud in a number of spectral channels sounding different portions of the atmosphere in different spectral intervals, one can infer some of the height and optical thickness properties of the cloud. The following section shows preliminary results based on observations of the cloud from HIRS2 data on March 29, 10 GMT, 5 hours after the initial eruption, and March 30, 9 GMT.

4.2.2. Preliminary observations

From imagery of the infrared brightness temperatures for March 29 10 GMT, features associated with the eruption are observed in all the HIRS2 channels but channe. and 17, which sound the mid-upper stratosphere. In channel 8, the 11 μm window, an extremely cold cloud is observed. The coldest spot is at 17.07°N, 93.14°W about 2.3° East of El Chichón, with a brightness temperature of 195.1°K. The cloud runs east-northeast, west-southwest with its maximum northeast extent given at 18.35°N, 91.59°W, with a 229.6° brightness temperature, in channel 8, and maximum southwest extent given at 17.04°N, 95.40°W, almost coincident with El Chichón, with a 239.6° brightness temperature. Outside the cloud, the brightness temperature rises sharply to a typical value of 286.7°, which was taken at 17.19°N, 96.46°W. The brightness temperatures can be compared with the air temperatures measured at Ver . .az, Mexico, at 12 GMT, 29 March (Fig. 4.7).

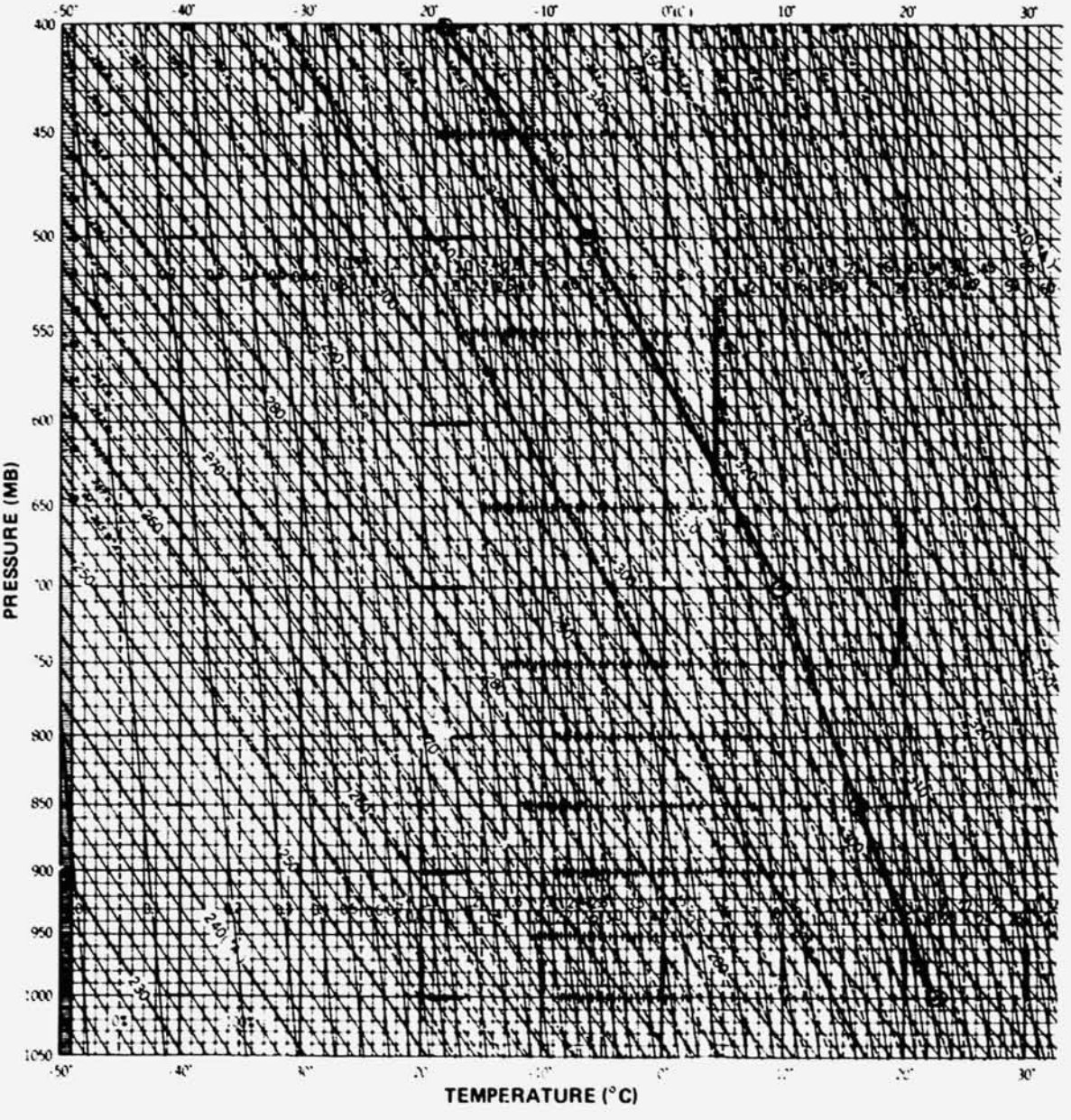

(A)

Figure 4.7. Temperature profile measured by radiosonde at Vera Cruz, Mexico, (19.15N, 96.12W) at 12 GMT, 29 March 1982.

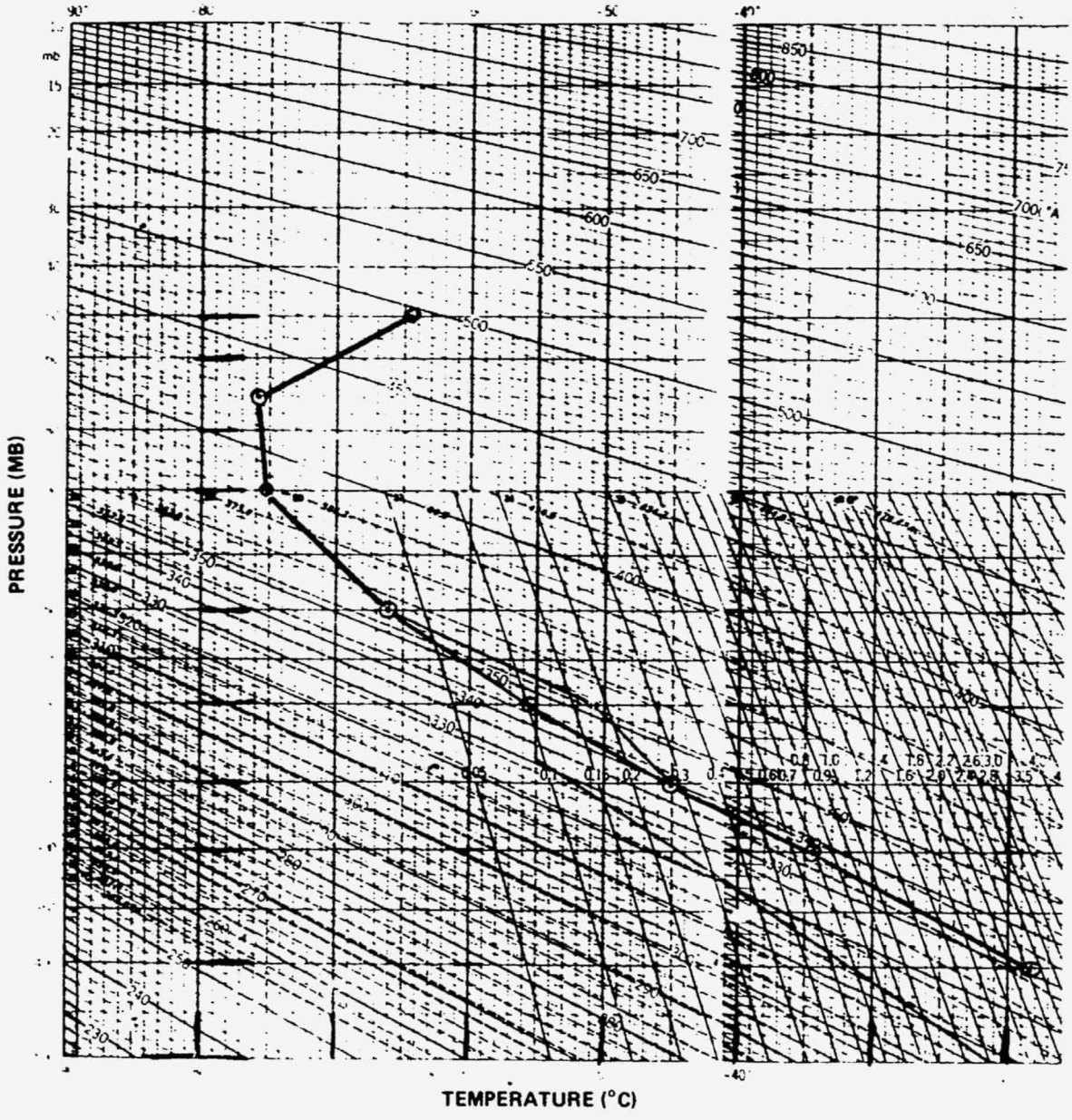

(B)

Figure 4.7. (Continued)

Brightness temperatures for all channels sensitive to the volcanic cloud are shown in Table 4.3, for both March 29 and March 30. On March 29, all observations are shown for the coldest spot (a), the southwest corner of the cloud located over the volcano (b), and a typical spot (c). In addition, observations in two window channels are shown for the northeast corner of the cloud (d). On March 30, the observations are shown for equivalent locations marked e-h. It is significant to note that on March 29 signals due to the cloud are clearly observed in stratospheric sounding channels 2 and 3, with the southwest edge of the cloud, located over the volcano, appearing warmer than the remainder of the field. Channel 2 is totally insensitive to observations lower in the atmosphere than 200 mb (12 km), indicating that the cloud must be at least in the upper troposphere.

If a cloud covers a spot with fractional cloud cover α, the radiance in channel i is given by

$$I_i = (1-\alpha)\, I_{i,CLR} + \alpha I_{i,CLD}$$

where $I_{i,CLR}$ is the radiance which would be seen if the field of view were clear and $I_{i,CLD}$ is the radiance which would be observed if the cloud completely covered the field of view of the instrument. The cloud blocks contributions to the radiance emitted from beneath it which would otherwise be observed by the channel. In general, clouds are in the troposphere and appear colder than the air beneath them. Therefore clouds in general appear cold. The warm spot over the volcano seen in channels 2 and 3 implies that if the cloud is at the same temperature as the atmosphere, either the cloud immediately above the volcano is higher in the stratosphere than the surrounding clouds, which would increase $I_{i,CLD}$, or the air in the stratosphere above the volcano is warmer than its ambient values, which would increase both $I_{i,CLR}$ and $I_{i,CLD}$.

The coldest spot appears increasingly colder as we go from channel 2 to 8, in the order of decreasing atmospheric optical depth from the satellite to the cloud. This is consistent with mixing in decreasing amounts of the warm stratosphere above the cloud with increasing spectral frequency. The brightness temperatures in the 4.3-3.7 μm region, seen in channels 13-19, are consistently

Table 4.3
HIRS Brightness Temperatures

CH	March 29 Coldest[a]	SW[b]	Typical[c]	NE[d]	March 30 Coldest[e]	SW[f]	Typical[g]	NE[h]
1			232.3					
2	217.0	221.6	218.1		217.4		218.0	
3	216.9	221.3	217.5		214.2	216.3	217.4	
4	202.3	218.9	231.3		216.8	223.5	231.0	
5	201.3	228.6	245.0		220.7		246.7	
6	198.5	231.6	254.1		223.6		259.4	
7	196.6	235.4	263.7		228.4		272.4	
8	195.1	239.6	286.7	229.6	242.4	248.8	287.0	268.0
9	213.6	228.8	266.9		247.3		273.1	
10	213.3	250.2	279.7		252.6		286.6	
11	197.3	231.9	251.7		232.3		261.6	
12	197.8	236.5	248.8		222.4		241.4	
13	205.1	255.0	275.6		258.0		283.2	
14	205.6	246.4	266.3		248.2		269.9	
15	210.1	234.1	250.9		233.9		251.2	
16	217.6	224.3	230.3		222.5		228.8	
17	–	–	–		–	–	–	
18	208.6	262.0	282.6	232.9	273.9	281.5	291.1	282.6
19	212.1	265.6	283.0		277.6	282.3	290.9	

a) 17.07°N 93.14°W
b) 17.04°N 95.40°W
c) 17.19°N 96.46°W
d) 18.35°N 91.59°W
e) 23.37°N 89.42°W
f) 22.28°N 92.41°W
g) 21.41°N 94.50°W
h) 23.94°N 88.17°W

warmer than in the 15 μm region. This implies that the cloud has bulk emissivity (ϵ) less than 1 at least in some spectral region. If αe were equal to 1, both the long and short wave window channels should have brightness temperatures nearly equal to the temperature of the cloud. The sum of ϵ plus ρ, the reflectivity of the cloud, $+\tau$, the transmissivity of the cloud equals 1. For non-unit ϵ, the cloud radiance consists of ϵ of the black cloud radiance, plus ρ of the very cold reflected space radiance, plus τ of the very warm transmitted clear column radiance. If ϵ is less than 1, then the brightness temperatures associated with the shortwave channels would always appear warmer than equivalent longwave temperatures because of mixing of the apparent brightness temperature from mixed radiance fields is weighted more toward the warm brightness temperature at the higher frequencies. This is consistent with the higher brightness temperatures at high frequencies. In addition, the higher brightness temperatures at high frequencies may imply that the cloud has higher emissivity in the long wave region than in the short wave region. The same phenomenon is observed in the spot above the volcano to even a larger degree.

On March 30, about 24 hours later, the cloud has approximately the same shape but has moved about 5°N and 3°E from its location on the day of the eruption. El Chichón appears to be cloud free at this time. The coldest spot has likewise translated by about the same amount. The appearance of the cloud in the infrared channels is quite different from the previous day, however. No warm spot exists in channels 2 and 3 and the cloud can barely be observed in channel 2. On the other hand, the signal of the coldest spot of the cloud is larger in channel 3 than in the previous day.

The cloud effects in the other longwave channels, 4-8, are clearly much less than in the previous day. Not only is the effect of the cloud smaller in each channel than on the previous day, but the brightness temperature in the coldest spot increases with decreasing optical depth, which is counter to the trend of the previous day. Because of the extreme cold temperature in channel 8 on March 29, it is almost certain that the coldest spot was completely covered by an optically thick cloud for the long wave channels. On the other hand, on March 30, $\alpha(1-\tau)$ must be considerably less

than 1 for the long wave channels, even in the coldest spot. The short wave channels 13-16 and 18, 19 show the same trend. In addition, the brightness temperatures in the short wave channels in the cloudiest spot are much warmer than in equivalent long wave channels. This is consistent with $\alpha(1-\tau)$ considerably less than 1, and in addition, with τ, the transmissivity, increasing with decreasing wavelength.

No signal attributable to El Chichón was observed in any MSU channel on either day. This may be in part due to the lower spatial resolution of the channels. In addition, no apparent signal was observed in any HIRS2 channel in the next satellite pass, March 30, 20 GMT.

4.2.3. Future plans

More comprehensive studies of the effects of El Chichón ejecta on retrievals of atmospheric temperature, sea surface temperature, and cloud fields will be done for a long period of time commencing with March 1982 in order to assess the effects of volcanic eruption on retrieved atmospheric temperature profiles and sea surface temperatures and to track the volcanic cloud and obtain its properties. Of primary interest is whether accurate sea-surface temperatures can be obtained from HIRS2, even under the H_2SO_4 aerosol cloud caused by the volcano.

J. Susskind

References (Section 4.2)

Kornfield, J., and J. Susskind, 1977: On the effect of surface emissivity on temperature retrievals. *Mon. Wea. Rev.*, 105, 1605-1608.

Susskind, J., J. Rosenfield, D. Reuter, and M. T. Chahine, 1982: The GLAS Physical Inversion Method for Analysis of HIRS2/MSU Data. *NASA Technical Memorandum 84936.* Goddard Space Flight Center, Greenbelt, MD 20771.

4.3. VAS ON GOES

4.3.1. Expected effects

The VISSR Atmospheric Sounder (VAS) is a 12-channel radiometer located on the operational geosynchronous GOES satellites. Twelve VAS channels are located in the 15 and 4.3 μm CO_2 bands, the 6.7 and 12 μm H_2O bands, and the 11 and 3.9 μm windows. Consequently, the spectral effects of El Chichón on the VAS channels will be the same as on the corresponding HIRS channels (Section 4.2). VAS data is archived routinely at the University of Wisconsin (UW) and occasionally by the VAS Demonstration at GSFC. NOAA's operational VISSR schedule rarely permits 12-channel VAS data collection from low latitudes. VISSR operations do permit hourly 3-channel scans of the globe in the 11 and 12 μm split window channels, coupled with either the 3.9 μm window or the 6.7 μm upper-air water vapor channel.

a) The VAS split window channels are used to estimate sea surface temperature (SST). An empirical regression formula developed by UW for SST along the East Coast of the United States is:

$$SST = 2.23\, T_{11}^{*} - 1.23\, T_{12}^{*}, \qquad (1)$$

where T_{11}^{*} and T_{12}^{*} are the apparent temperatures in the 11 μm and 12 μm channels, respectively. The effects of El Chichón on VAS SST should be detectable at the $\pm 1^{\circ}C$ level, provided there are no other clouds in VAS' 15 km footprint. At low latitudes, the 3.9 μm window is much too affected by reflected sunlight to be useful during daylight operations.

b) The VAS 6.7 μm water vapor channel is like the familiar METEOSAT band, with its radiance representing the average brightness of the top few millimeters of the atmospheric water vapor. The 6.7 μm radiance normally arises from a layer a few hundred millibars thick, centered at a level between 300 and 500 mb. However, molecular water vapor injected by El Chichón into the lower stratosphere would appear as an unusually cold

feature in the 6.7 μm radiance field. For example, 1 mm of precipitable water in the layer from 50 to 250 mb (mixing ratio about 0.1 gm/kg, or relative humidity about 50% at 220 K) would appear as a feature about 10°K colder than the surrounding scene.

4.3.2. Observed effects

UW has been monitoring VAS SST along the East Coast during 1982. They report a few degree depression in the VAS SST at buoys located east and west of the Florida peninsula during June 1982, and smaller depressions are observed during mid-summer which are consistent with AVHRR SST depressions.

Because VAS observations are oriented towards the United States, they rarely extend below 30°N. By chance, some 3-channel low-latitude scans are available from the VAS Demonstration at GSFC, taken at 1530, 1600 and 1630 GMT on 6 and 8 April 1982, which is a few days after the main eruption of El Chichón.

a) On both days, an unusual low cloud was observed in the 11 and 12 μm VAS radiances. The cloud was about 10°K colder than the surrounding clear areas, and it obscured the quadrant northwest of El Chichón. Fig. 4.8 shows this cloud's effect on the VAS SST calculated over the entire scene from the split window radiances observed at 1600 GMT on 6 April 1982. El Chichón's location is marked by a "+". The "SST" is 5°C less than the surroundings near Mexico and over the Gulf of Mexico. There is no clear sign of an effect on VAS "SST" further west of El Chichón, where stratospheric particulates might be expected.

b) Fig. 4.9 shows the corresponding 6.7 μm image. There is an unusual cool (7°K lower) feature in the warm cloud-free streak over Mexico, to the west of El Chichón. This molecular water vapor feature is more compact than the contemporaneous stratospheric features

Figure 4.8. The sea surface temperature measured by VAS from GOES-5 at 1600 GMT on 6 April 1982. The SST grey scale is at the top.

ORIGINAL PAGE
BLACK AND WHITE PHOTOGRAPH

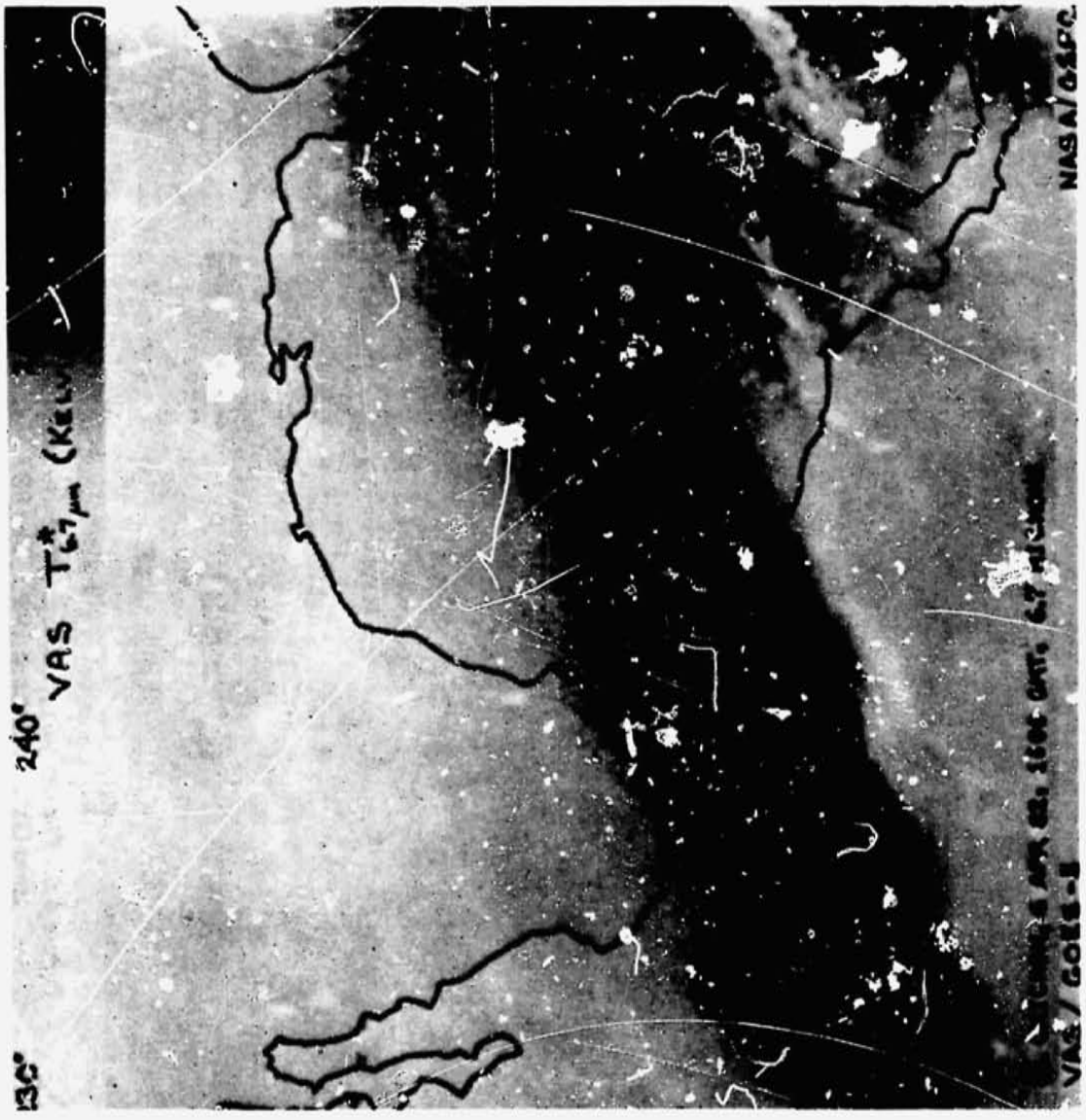

Figure 4.9. The VAS apparent temperature measured in the 6.7 μm band from GOES-5 at 1600 GMT on 6 April 1982. The temperature grey scale is at the top.

observed in the SBUV/TOMS images (Section 4.4). One millimeter of precipitable water over an area of 250 by 400 km would be 10^8 tons of H_2O. The feature is not identifiable in the 6.7 μm image on 8 April.

Without a more continuous series of VAS images, one cannot be certain that either of the VAS-observed features was actually ejected by El Chichón.

4.3.3. Corrections

Because the VAS instrument is normally dedicated to studies over the United States, where the effects of El Chichón are comparable to VAS' radiometric errors (±1°K brightness temperature), there is no need to correct VAS soundings for El Chichón's ejecta.

4.3.4. Further research

Future volcanic erruptions in the Western Hemisphere should be monitored more deliberately with short (10 minute) interruptions of the operational VISSR schedule to acquire 12-channel VAS soundings over a 10° latitude band every hour. A volcano watch of this sort would be basically the same as hurricane and severe storm watches already permitted by NOAA. During such a volcano watch, the VAS Demonstration facility at GSFC should collect VAS radiances and provide immediate data processing for scientific investigators.

D. Chesters

References (Section 4.3)

Chesters, D., L. W. Uccellini, H. Montgomery, A. Mostek, and W. Robinson, 1981: Assessment of the first radiances received from the VISSR Atmospheric Sounder (VAS) instrument. NASA Tech. Memo 83827, Goddard Space Flight Center, Greenbelt, MD 20771 (NTIS 82N19730).

4.4. TOMS AND SBUV TOTAL OZONE RETRIEVALS AND VERTICAL PROFILES

4.4.1. Total ozone determination

4.4.1.1. Theoretical effects

a. Gaseous absorption

The TOMS and SBUV instruments measure total ozone by observing the radiance of the back-scattered atmospheric sunlight in the Hartley absorption bands of ozone. In the unperturbed atmosphere other known species which could interfere with total ozone retrievals have abundances $<10^{-4}$ of the ozone abundance and do not cause retrieval errors. Volcanic clouds contain two sulfur compounds, SO_2 and CS_2, which can directly interfere with ozone if the quantity is great enough. The spectra of SO_2 and CS_2 from Wu and Judge (1981) are shown in comparison with ozone in Fig. 4-10. Three of the wavelengths used by SBUV and TOMS for total ozone measurement are indicated by the arrows. The retrievals use the wavelength pairs 312.5/331.2 nm and 317.5/339.8 nm, referred to as the A- and B-pairs, respectively. It is clear that either constituent will produce erroneously high ozone amounts if not corrected. The absorption coefficients (base e) for 0_3, SO_2 and CS_2 at the total ozone wavelengths are listed in Table 4.4 together with the ratios of SO_2 and CS_2 to ozone absorption coefficients. The differences in the absorption coefficients for the A- and B-pairs appear on the last two rows. Although SO_2 and CS_2 are expected to have significant temperature dependencies, measurements at low temperatures corresponding to El Chichón cloud exist only for CS_2 (Wine et al., 1981). The effects of SO_2 are seen to be strong at the shortest two wavelengths which are the primary ones for the ozone measurement. One unit of SO_2 is equivalent to about 2.5 units of ozone. A unit of carbon disulphide is roughly equivalent to that of ozone. At 331.2 and 339.8 nm SO_2 absorption is small compared with ozone absorption while CS_2 is considerably larger. The true SO_2 cross sections at El Chichón cloud altitude of 27 km will be smaller than the above values due to the temperature effects, but the amount is at present unknown.

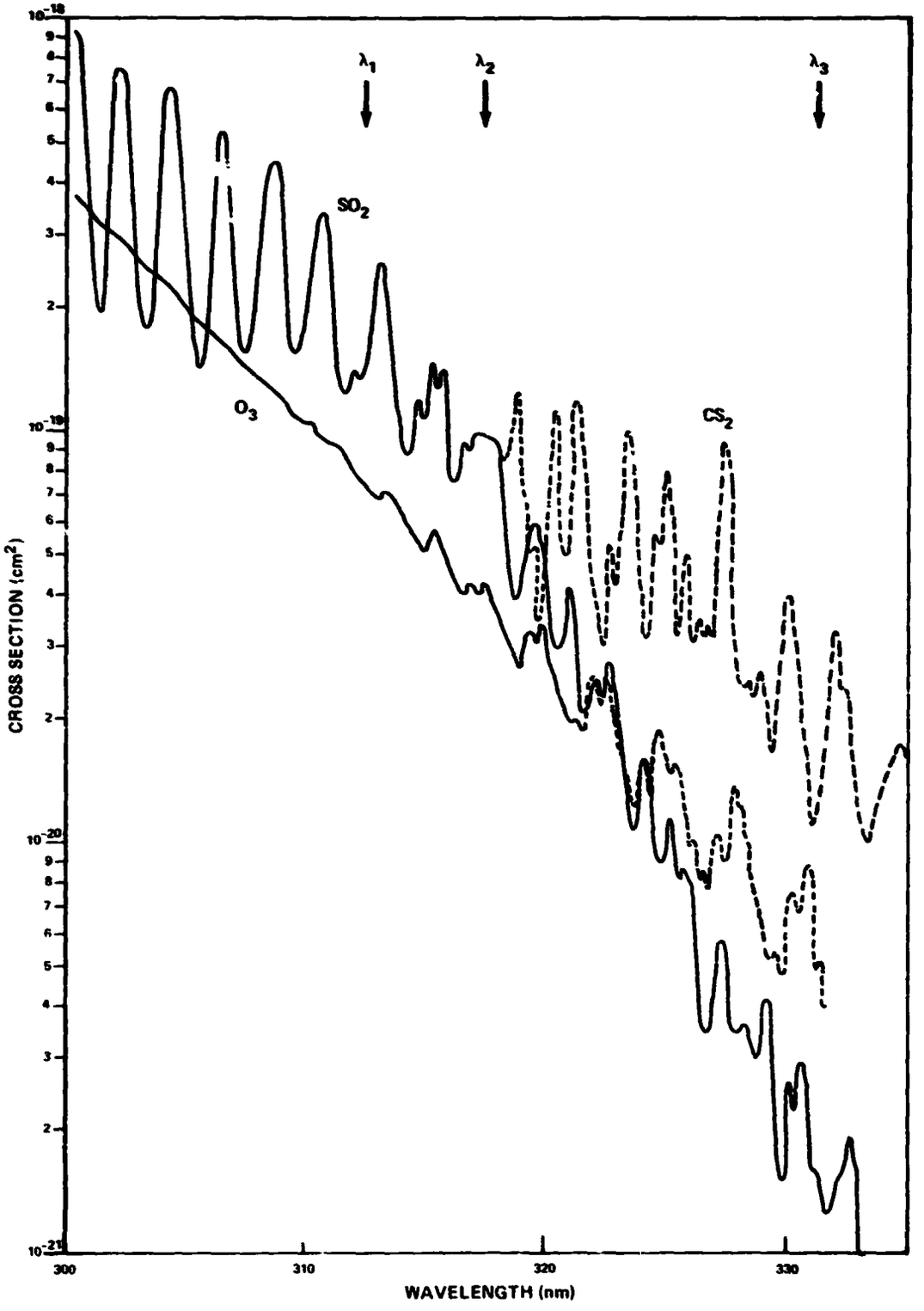

Figure 4.10. Cross section of ozone, sulfur dioxide and carbon disulphide in the spectral region used by SBUV and TOMS for total ozone measurements.

Table 4.4
Absorption Coefficients (Base e) at TOMS and SBUV Wavelengths
in Units of cm^{-1} of Gas at NTP

Wavelength (nm)	$\alpha\ O_3$ (229 K)	$\alpha\ SO_2$ (294 K)	$\alpha\ CS_2$ (254 K)	$\frac{\alpha\ SO_2}{\alpha\ O_3}$	$\frac{\alpha\ CS_2}{\alpha\ O_3}$
312.5	1.777	4.09	1.602	2.30	0.902
317.5	0.9264	2.36	1.274	2.55	1.375
331.2	0.1676	0.042	0.632	0.251	3.771
339.8	0.0405	0.019	0.080	0.469	1.975
360.0	0	0	0	–	–
380.0	0	0	0	–	–
A-pair	1.609	4.048	0.970	2.52	0.603
B-pair	0.8859	2.341	1.194	2.64	1.348

b. Aerosol scattering

The present retrieval model assumes a multiple scattering Rayleigh atmosphere with a Lambertian reflecting lower boundary. The peak contribution to backscattered radiances is found in the lower troposphere at tropical latitudes. A dense aerosol cloud in the stratosphere can scatter photons to space without having passed through the ozone below the cloud and thus produce an underestimate of the total ozone. However, if the particles also absorb, this effect is counteracted. Dave (1978) has studied these effects for typical stratospheric and tropospheric aerosol distributions. He finds very slight ozone underestimations for non-absorbing aerosols but significant overestimations for absorbing aerosols. Since El Chichón cloud is higher and denser than Dave's assumed aerosol distributions, it will be necessary to carry out radiative transfer calculations to determine the particular effects.

4.4.1.2. Observed effects

El Chichón cloud produced a strong perturbation in TOMS radiances at the two shortest wavelengths (Krueger, 1983). This is shown in Fig. 4.11, which portrays the logarithm of the ratio

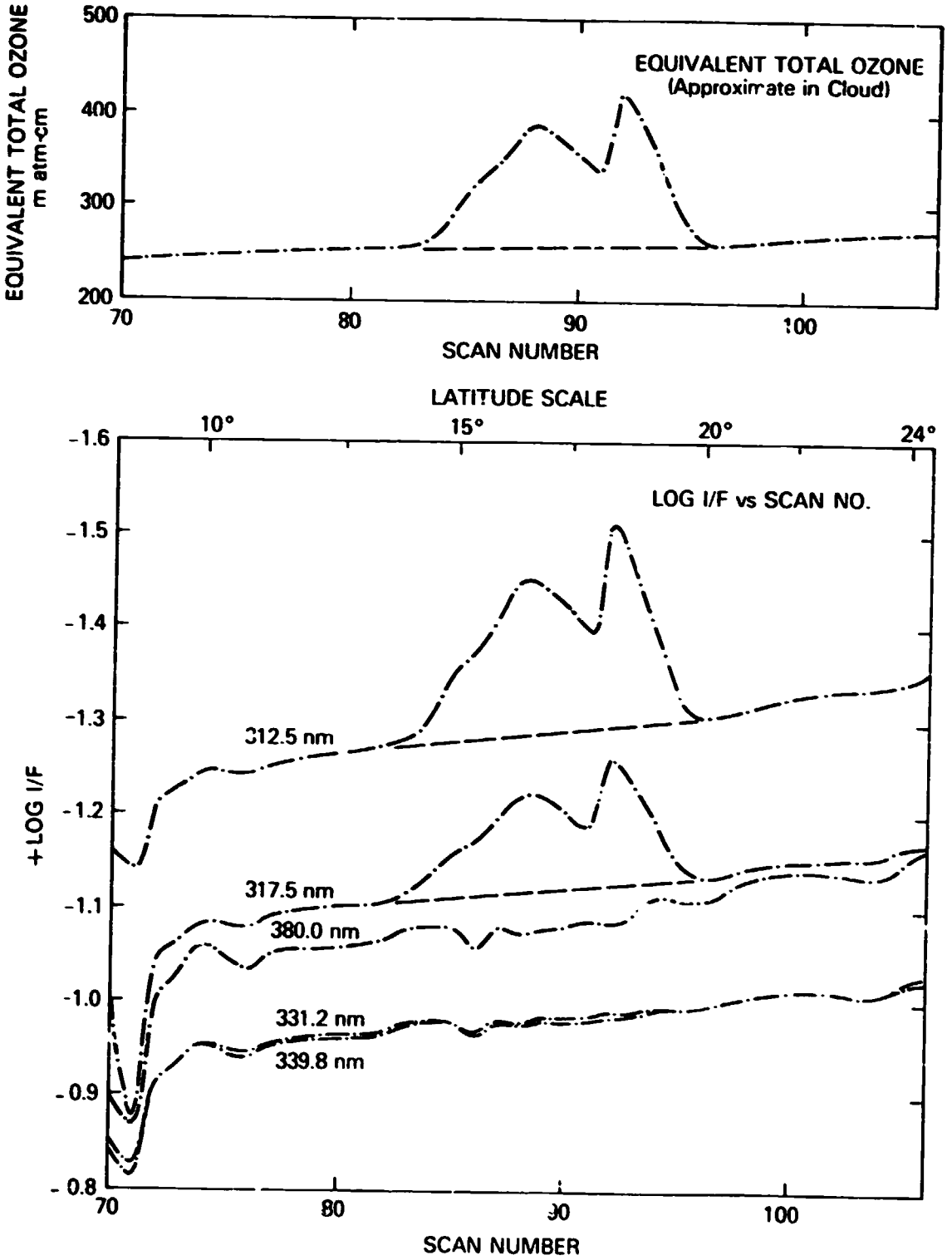

Figure 4.11. Apparent total ozone amounts in a trace across El Chichón cloud (upper). Equivalent optical depth of atmosphere in same trace across cloud at five TOMS wavelengths (lower).

of radiance (I) to solar irradiance (F) at five of the TOMS wavelengths for a trace across the early cloud. The spectral signature is consistent with the presence of SO_2 and inconsistent with CS_2, as can be seen by inspection of Table 4.4. The longer wavelengths show only slight perturbations due to aerosols. Thus by far the largest effect is a severe overestimation of total ozone by more than 200 m atm cm due to the SO_2 absorption (see Fig. 2.6 in section 2). As the cloud was sheared by the winds and the SO_2 was chemically lost, the ozone retrieval error diminished.

A second effect was that the difference between A- and B-pair ozone retrievals was large over the cloud. If the SO_2 absorption coefficients in Table 4.4 were correct and the dust was non-absorbing, the difference should be small. An explanation will require low temperature SO_2 cross section data and radiative transfer calculations.

A third effect, found after about 2 months was scan angle dependence of the TOMS ozone retrievals with lower values obtained at nadir than at large scan angles. This effect is not understood but probably is due to aerosol effects.

4.4.1.3. Correction of data

The total ozone retrieval errors due to the presence of SO_2 diminish rapidly as the volcanic cloud is dispersed by winds. An upper limit to the total ozone error is obtained by assuming no chemical conversion, while the cloud is mixed uniformly within a latitude zone. For example, if El Chichón injection of SO_2 is mixed uniformly within the latitude zone 0°-30°N, the average bias in the estimate of ozone is 2.3 m atm cm. Given a determination of the rate of loss of SO_2, it should be possible to correct the zonal mean total ozone with adequate precision for most purposes.

4.4.1.4. Further research

a. Analysis of existing data

The properties of the cloud will evolve with time. Effort is needed to determine the best cloud signature and to use this to locate both the tropospheric and stratospheric clouds as a function of

time. This will permit a determination of the rate of loss of SO_2 which is required for any correction scheme. Aerosol properties may also be inferred by comparison with surrounding areas during the time when a discrete cloud can be identified.

b. Comparison with other satellite data

The cloud boundaries differ between those derived from TOMS, AVHRR, and VAS observations. This may be due to wavelength effects but also could result from altitude differences across the cloud. This needs to be explored as a possible way of discriminating cloud altitude. In addition the SBUV continuous scan data need to be examined for similar reasons as noted in the ozone profile section and also to determine whether constituents other than SO_2 were present.

c. Cross section data

Sulfur dioxide cross sections at stratospheric temperature and pressure conditions need to be measured.

d. Radiative transfer calculations

The conditions of an absorbing-scattering aerosol cloud near the ozone maximum have not been simulated. Off-nadir radiative transfer calculations have not been made for TOMS under high aerosol conditions. These calculations are essential for understanding El Chichón effects.

A. J. Krueger

4.4.2. SBUV ozone profiling

4.4.2.1. Theoretically expected effects

The effect is very sensitive to the altitude of the volcanic cloud – the higher the cloud the larger the effect. Aerosols that rise above the ozone density peak (~25 km in tropics) produce a far greater effect than those that lie below the peak. Therefore, the effect of El Chichón on SBUV profiling should greatly exceed that of Mt. St. Helens, which injected aerosols in the lower

stratosphere only. If El Chichón cloud was located at 27 km, the four shortest SBUV bands, located below 290 nm, will not be affected. The effect at 292 nm is strongly dependent on the aerosol altitude profile and the distribution of ozone in or above the aerosol layer – the higher the aerosol layer in relation to the ozone layer the larger the effect. If we assume that little aerosol was injected above 30 km, the effect on 292 nm radiances should be less than 5% (assuming tropical ozone profiles). For longer SBUV profiling bands located at 298, 302 and 306 nm the predicted effect of the aerosols is extremely large ~30-50%. If the SBUV profiling algorithm ignores the presence of such a large perturbation, the ozone profiles derived in 1-5 mb region would be in error by 5-10%; below 5 mb the error would increase rapidly, perhaps becoming as large as 50% in the 10-20 mb region of the atmosphere. These results are, however, preliminary and more work needs to be done to understand the effects.

Dave (1978) made an extensive modeling study of the effects of stratospheric aerosols on the estimates of total amount of ozone as measured by SBUV. His aerosol model, however, was not the same as El Chichón aerosol. Dave's aerosol profile had a maximum at 20 km, whereas El Chichón's maximum concentration was at 26 km. Also, Dave's maximum aerosol optical thickness was 0.06, as compared with an El Chichón value of 0.2 (Fig. 3.2). This study indicated that for non-absorbing aerosols the effect on estimates of total amount of ozone is small but can become quite significant for absorbing aerosols.

The shape of the scattering phase function strongly affects the amount of scattered light, but it is fairly well understood. Since the SBUV is a nadir viewing instrument, the scattering angle is the same as 180° minus the solar zenith angle. Based on calculations done by M. King and John DeLuisi (private communication), the largest effect would be for overhead sun and the minimum effect should occur at a solar zenith angle of ~50°, with variations of the order of a factor of five. Some interesting anomalies have been predicted for the aerosol phase function – showing oscillations at scattering angles of ~160° – that should be observable in SBUV radiances.

The single scattering albedo of the volcanic aerosols for the ultraviolet spectrum is, perhaps, the greatest unknown in assessing the impact of the volcano on SBUV and TOMS. Even a weak absorption, if present, would significantly reduce the effect of aerosol on SBUV radiances for the shorter wavelengths. Indeed, for an aerosol with imaginary part of index of refraction of ~0.05, the aerosol might appear neutral at longer wavelengths–producing no observable signatures in the back-scattered radiances.

The presence of SO_2 will also cancel out the effect of aerosols and could, indeed, reverse the effect – producing a decrease of radiances. However, preliminary results indicate that the stratospheric SO_2 is not large enough to cancel out the scattering effects. Even if it did at some wavelength, the effect would vary dramatically with wavelength, following the unique SO_2 absorption spectrum.

4.4.2.2. Further research

No study has so far been done that predicts the effect of an aerosol layer located above the ozone density maximum on the SBUV radiances – particularly those that are strongly multiply scattered. Existing studies were either done for a very thin aerosol layer at ~20 km (Dave) or for clouds located in the troposphere (Dave, Fraser). These studies cannot be used to predict the effect when the aerosol layer is above the ozone layer.

The effect of a large perturbation of the longer wavelength radiances on the upper level profile retrieval is not known and should be studied.

It is extremely important for the analysis of SBUV/TOMS data that we know the single scattering albedo of El Chichón aerosols on ultraviolet wavelengths. Some measurements already exist but are not sufficient (Patterson, 1981).

Optical properties of the volcanic aerosol can be obtained by analysing the SBUV/TOMS data. Such a study could reveal the phase function of the aerosols, its optical depth, altitude distribution,

and amount of SO_2 present. More importantly, if one can find a way to track the cloud over the globe and the way is disperses, it may be possible to correct the SBUV and UMKEHR ozone data using those results.

P. K. Bhartia

References (Section 4.4)

Dave, J. V., 1978: Effect of aerosols on the estimation of total ozone in an atmospheric column from the measurements of its ultraviolet radiance. J. Atm. Sci., 35, 899-911. 1978.

Krueger, A. J., 1983: Sighting of El Chichón sulfur dioxide clouds with the Nimbus 7 Total Ozone Mapping Spectrometer. Science (in press).

Patterson, E. M., 1981: Measurements of the imaginary part of the refractive index between 300 and 700 nanometers for Mount St. Helens Ash. Science, 836-838.

Wine, P. H., W. L. Chameides, and A. R. Ravishankara, 1981: Potential role of CS_2 photooxidation in tropospheric sulfur chemistry. Geoph. Res. Lett., 8, 543-546. 1981.

Wu, C. Y. R. and D. L. Judge, 1981: SO_2 and CS_2 cross section data in the ultraviolet region. Geophys. Res. Lett., 8, 769-771.

4.5. ERB ON NIMBUS-7

The Earth Radiation Budget (ERB) experiment on Nimbus-7 measures upward flux in two broad wavelength bands:

1) $0.2 - 50\ \mu m$

2) $0.2 - 3.8\ \mu m$

The instantaneous field-of-view extends beyond the earth's limb. The difference between total and solar upward fluxes is the long wave upward flux. The major influence of stratospheric aerosols is on the solar reflectivity, which is anticipated to increase slightly for regions covered by El Chichón aerosol cloud. The total change in reflected energy is expected to be 5-10 W/m^2 for

El Chichon compared with 200-250 W/m^2 mean solar reflection, and this enhancement could possibly be detected if the time series is analyzed carefully. Unfortunately, ERB data processing is currently at 1980, and data pertinent to El Chichón will not be available for at least another year. There is also no gain to be expected from analyzing the data out of sequence, since comparison with previous data is the only way to detect the order of the change anticipated.

The effect of the cloud in the long wave is more difficult to assess. However, since the optical depth of H_2SO_4 in the long wave is much less than in the solar and the high aerosol cloud is at a temperature close to the middle troposphere, no significant effect is anticipated.

Figure 4.12 shows the additional reflection of solar energy to be expected from a layer of 75% H_2SO_4 aerosols of visible (0.55 μm) optical depth of 0.1. For small optical depths, the response is almost linear and the figure can be used to scale the effect of El Chichón cloud, which had an optical depth of 0.2-0.25 in a band extending from 0°N-30°N in the summer of 1982.

The cloud is expected to diffuse over time and the radiative perturbation is expected to decrease. It must be stressed that the Fig. 4.12 only supplies the estimated initial radiative perturbation. If through some physical response, there is a significant change in tropospheric cloudiness as a result of this radiative perturbation, El Chichón signal will probably not be detected in the zonal mean reflectivity.

Although the radiative perturbation is only marginally detectable, the aerosol cloud could significantly influence the mean surface temperature. Application of the radiative model to the GLAS Multi-Layer Energy Balance Model with an assumed two-year residence time for the aerosol, indicates that the peak response of climate should occur approximately 2.5 years after the aerosol layer has reached its production peak. The peak effect on the hemispheric mean surface temperature will be between 0.3 and 0.5°C depending on the assumed parameters and climate feedback processes. The low latitudes will show the earliest response if the aerosol

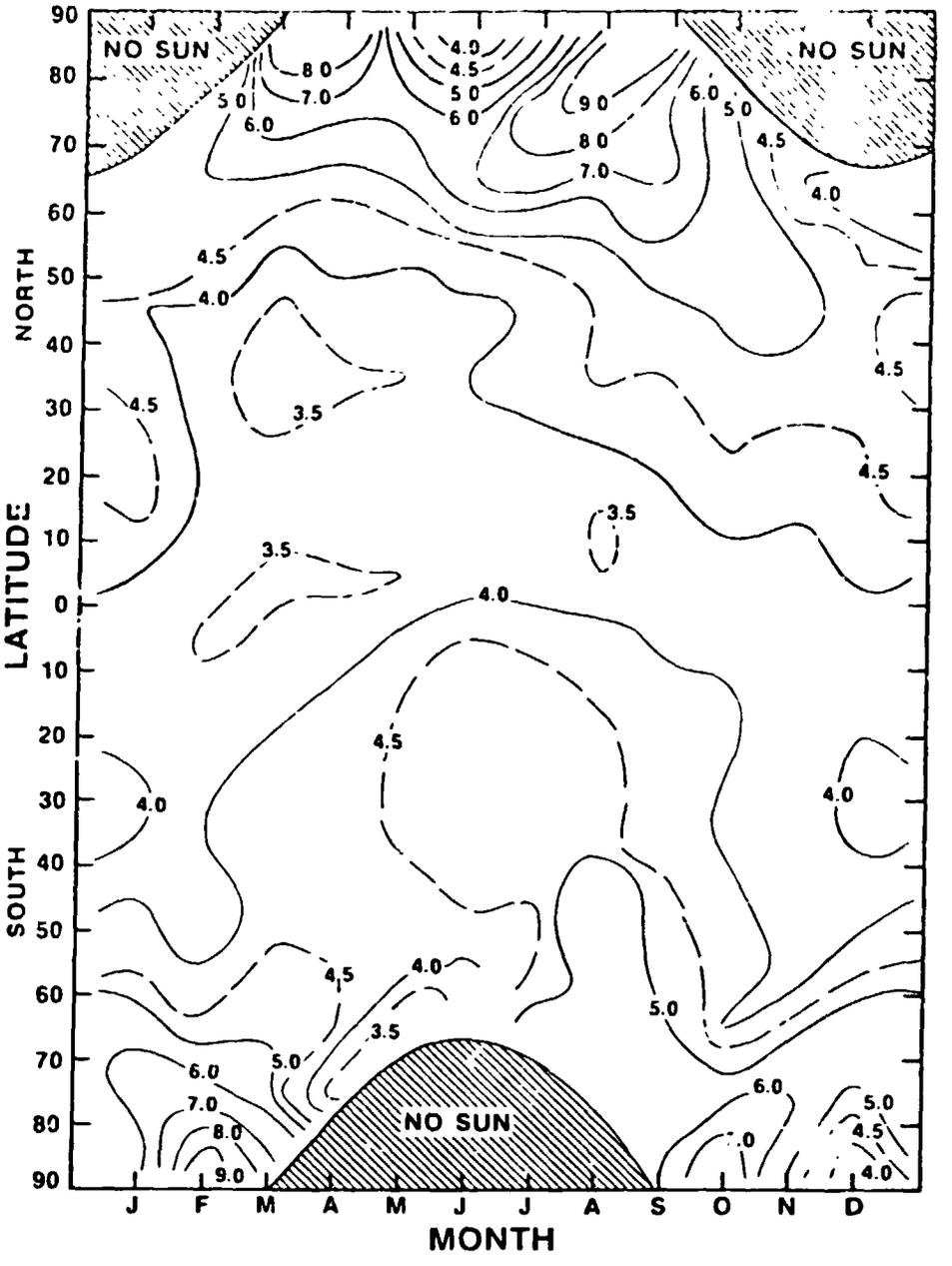

Figure 4.12. Reduction in mean monthly solar energy absorbed (Wm^{-2}) with addition of aerosol layer of $\tau_{vis} = 0.1$. (Harshvardhan, 1979).

layer is largely confined to those latitudes, as now seems to be the case. There will then be a cascading effect on higher latitudes, with the peak response appropriately delayed.

Harshvardhan
M. D. Chou

References (Section 4.5)

Harshvardhan, 1979: Perturbation of the zonal radiation balance by a stratospheric aerosol layer. J. Atmos. Sci., 36, 1274-1285.

4.6. CZCS PRODUCTS

The data processing for the Coastal Zone Color Scanner (CZCS), as part of the scheme to eliminate atmospheric path radiance consisting of both Rayleigh and aerosol contributions, begins by calculating the Rayleigh radiance for the bands at 443, 520, 550 and 670 nm, and subtracting that radiance from the aperture radiance measured by the sensor. The algorithm for the atmospheric correction then utilizes an assumed aerosol scattering efficiency of 1 for the four previously mentioned wavelengths, and the assumption that the reflected radiance from the surface at 670 nanometers is negligible in the case of clear water. The algorithm searches for the clearest or bluest water and then calculates a relative scattering efficiency of the aerosol at 443, 520 and 550 based on a relative scattering efficiency of 1 at 670 nanometers.

Although aerosol path radiances are calculated for all four spectral bands in the removal of the atmospheric contributions of CZCS data, only the aerosol path radiance at 670 nanometers is retained and archived as part of the Level II product. The aerosol path radiance for the channel at 670 nanometers is retained (as part of the pictorial and the magnetic tape product) in a range of 0 to 1.5 milliwatts per square centimeter micrometer steradian. This path radiance has shown that aerosols are quite spatially variable and that extrapolation from one area of the picture to another, such as from water to adjacent land, would probably not be valid

At the southern end of Baja California in the latitude range most affected by the El Chichón dust, an area has been selected and a number of scenes have been requested for priority processing through to Level II, so that the aerosol path radiance in this area might be compared wi[illegible]t from previous years in the same area. Since the CZCS on Nimbus-7 was launched in 1978, we have a data set from the summer of 1979, 80 and 81, prior to the El Chichón eruption, that can provide a comparison of the aerosol path radiance for three years running to that after the El Chichón eruption. The data from the orbits in question is being processed now as rapidly as possible by the Information Processing Division at NASA/GSFC, and the comparison will be made as soon as the Level II product is available.

W. A. Hovis

4.7. SMMR PRODUCTS

The Scanning Multichannel Microwave Radiometer (SMMR) on Nimbus-7 is a ten-channel microwave radiometer that measures brightness temperatures at 6.6, 10.7, 18, 21, and 37 GHz in dual polarization. The conical scanning geometry of SMMR is such that the instrument views the earth's surface at a constant incidence angle of about 50°. The spatial resolution of the instrument is proportional to wavelength and varies from about 155 km at 6.6 GHz to about 30 km at 37 GHz

Except possibly for a period within 12 hours of a major El Chichón eruption, ejecta will not be discernible by satellite microwave observations. To explain the negligible effect of the El Chichón aerosols, a comparison can be made with the empirical results of SMMR observations of liquid water clouds. The microwave index of refraction of water is large, and one anticipates the index of refraction of El Chichón aerosols that reside in the stratosphere a few months after the last eruption is large, also. The cloud drops are several orders of magnitude smaller than the microwave wavelength (~ 1 cm), and El Chichón particles are even an order of magnitude smaller than the cloud drops (section 3.2). Attenuation of microwave radiation by such clouds is dominated by absorption,

rather than by scattering (van de Hulst, 1957). The total absorption is proportional to the cloud mass in a vertical column. The 37 GHz, horizontal polarization channel of the SMMR is the most sensitive to clouds over water. Since the noise-equivalent-temperature of the channel is about 1K, the minimum detectable cloud mass is about 1 mg cm^{-2} (Chang and Wilheit, 1979). The mass of El Chichón cloud a few months after the last eruption was 0.006 mg cm^{-2} (section 3.2), which is far too small to be detected by SMMR.

The sea surface temperature derived from the SMMR observations can possibly be used to verify the NOAA operational SST derived from infrared radiances. The SMMR SST can be obtained globally for monthly periods. Then, the deviation between the microwave and infrared SST's can be used to outline the geographical extent of the El Chichón stratospheric cloud, since the infrared radiances are affected by the cloud, whereas the microwave radiances are not.

P. Gloersen

References (Section 4.7)

Chang, A. T. C. and T. T. Wilheit, 1979: Remote sensing of water vapor, liquid water, and wind speed at the ocean surface by passive microwave techniques from Nimbus 5 satellite. Radio Science, 14, 793-802.

van de Hulst, H. C., 1957: Light scattering by small particles. John Wiley and Sons, New York, 470 p.

4.8. MSS AND TM ON LANDSAT

The Multispectral Scanner (MSS) and the Thematic Mapper (TM) measure the radiance of sunlight scattered from the earth and its atmosphere in many spectral bands between 450 to 2300 nm. Characteristics of surface features on the earth are derived from these observations. The major

C-2

cause for atmospheric error in classifying surface features is the variable optical characteristics of atmospheric aerosols. An increase in amount of aerosols reduces contrast, reduces spatial resolution, and alters spectral signatures.

The effect of El Chichón aerosol on MSS and TM observations is expected to be less than effects due to the atmosphere that are routinely encountered. The aerosol effect can be related to its optical thickness. A few months after the last major eruption, El Chichón's stratospheric aerosol had stabilized with an optical depth of 0.2 for the spectrum 400-1000 nm in the latitude zone of 10°-30°N. If the aerosol diffuses over the entire northern hemisphere, the optical depth will be 0.1, or less. Its gradients would be weak with an expected uniform spatial distribution.

The dominant source of atmospheric error in characterizing surface features, however, would still be the tropospheric aerosol, concentrated within a few kilometers of the earth's surface. The mean value of that aerosol optical thickness is 0.5 and its standard deviation is about one-half of that over the eastern half of the United States during the summer. The stratospheric cloud would add an additional thin, uniform veil between Landsat and the ground. This veil is not expected to cause additional effects that are important in comparison with tropospheric effects that occur routinely.

R. S. Fraser

5. CONCLUSIONS

The last eruption of the El Chichón volcano occured on 4 April 1982 (day 94). The AVHRR and VISSR delineated the diffusion of the aerosols resulting from the volcano as they circled the globe during the next 3 weeks. The AVHRR sea surface temperature bias indicated that the stratospheric aerosols were mostly confined to the latitude band 10N-30N before diffusing north and south in July and later. SME and lidar observations placed the aerosol layer between 20 and 35 km altitude, with a weak layer between 18 and 20 km.

The effect of the stratospheric cloud on measurements of sea surface temperature depends on the sensor and its algorithm. Temperatures derived from the AVHRR observations were as much as 2.5°C lower than ship and buoy temperatures. The sea surface temperatures have not yet been derived for other infrared measurements (HIRS and VAS). Because the stratospheric cloud is essentially transparent to microwave radiation, SMMR and MSU measurements will not be affected by the cloud.

TOMS observations of the total amount of ozone in the region of the volcanic ejecta were seriously over estimated because of the absorption by SO_2. Krueger, however, has utilized the TOMS observations to estimate the total amount of SO_2 ejected by El Chichón. Both the stratospheric aerosols and SO_2 are expected to have significant effects on the vertical profiles of the ozone concentration, derived from SBUV observations.

The temperature and humidity profiles measured by the infrared sensors will be affected by the volcanic ejecta, at least in the more concentrated regions. VAS profiles have been restricted to the United States. The profiles already analyzed were taken before the cloud reached the U.S. When the cloud reaches the U.S., it would be less concentrated. Then the temperature perturbations are expected to be less than 1K, which is within the noise level. Chesters feels that the VAS temperature and humidity retrievals over the United States will not be affected by the stratospheric

cloud. Susskind, on the other hand, has seen large positive and negative temperature anomalies in the HIRS observations within a day of an El Chichón eruption and near to it. Small biases in the temperatures that persist after the stratospheric cloud becomes more tenuous may still have a significant effect on the retrievals.

The stratospheric cloud has a negligible effect on microwave observations and is expected to be small or routinely correctable for ERB, CZCS, MSS, and TM satellite observations.

In order to modify the satellite algorithms to account for the volcanic effects, additional work is required. The anomalies can be used, however, to measure the characteristics of the volcanic aerosols and dispersion.

6. RECOMMENDATIONS

Algorithms for some of the satellite sensors need to be modified in order to account for the effects of volcanic ejecta on radiant energy. The SBUV/TOMS measurements in the ultraviolet spectrum of the total ozone and its vertical profile are strongly affected by the residual stratospheric aerosols and trace gases. The radiation characteristics of the aerosols in ultraviolet light are poorly known, and the existing SO_2 absorption spectra are not accurate. Experimental data on both scattering and absorption characteristics are needed. With such data the radiative effects of stratospheric clouds need to be modeled. Then the effects of the aerosols can be accounted for in not only the ozone algorithms, but also for the infrared algorithms. It is recommended that the above studies and experiments be carried out.

The residual cloud remaining in the stratosphere causes an apparent decrease in the sea surface temperature measured in the infrared spectrum. Stowe is developing an algorithm to remove such a bias from the AVHRR data. Removal of this bias from the HIRS data presents a different problem and needs to be analyzed. SMMR measurements of SST are not affected by the volcanic cloud and can be used as a set of reference data. It is recommended that studies be made to account for El Chichón cloud on SST.

The temperature and humidity sounding algorithms for HIRS measurements require modification to account for the volcanic ejecta. Susskind intends to analyze the HIRS data carefully. His studies will indicate the requirements to derive accurate temperature and humidity profiles. It is recommended that such studies be made, and Susskind has indicated his intent to do so.

The satellite data already available can be used to provide more information about the effects of El Chichón eruption on the atmosphere. The amounts of trace gases and their vertical profiles may be derived from the SBUV measurements of the radiance with high spectral resolution in the spectrum λ 1600-4000Å. Krueger has already made preliminary estimates of the amount of SO_2

injected into the atmosphere from the TOMS data. Both SBUV and TOMS may possibly provide aerosol optical thickness data about aerosol particles smaller than a few tenths of a micrometer in diameter. Since volcanic aerosol effects have not been apparent in the TOMS data, all radiation parameters will have to be carefully accounted for in order to measure the aerosol effects. It is recommended that research be performed on the information that can be derived from satellite ultraviolet observations concerning volcanic ejecta, its composition, spatial extent, and decay characteristics.

The visible and near infrared radiances measured by AVHRR and VAS over water can be used to measure the geographical dispersion of aerosols. Stowe is investigating the possibility of doing this. Also, the geographical location of the stratospheric aerosol layer closely coincided with the region of sea surface temperature anomalies measured by AVHRR. The length of time such anomalies exist and their relation to the stratospheric layer are under investigation by NOAA scientists. It is recommended that such studies be continued concerning use of visible and near infrared observations to characterize the volcanic aerosols.

The satellite data, together with additional data from surface, aircraft, and balloon observations, provide a rich source to utilize in investigation of climatic effects, atmospheric diffusion, and the complex chemistry of the stratosphere.